Available online at www.sciencedirect.com

ScienceDirect

Geochimica et Cosmochimica Acta 278 (2020) 199–218

Geochimica et Cosmochimica Acta

www.elsevier.com/locate/gca

An SPO-induced CPO in composite mantle xenoliths correlated with increasing melt-rock interaction

Emily J. Chin [a,*], Vincent Soustelle [b], Yongsheng Liu [b]

[a] Scripps Institution of Oceanography, University of California San Diego, La Jolla, CA 92093, USA
[b] State Key Laboratory of Geological Processes and Mineral Resources, School of Earth Sciences, China University of Geosciences, Wuhan, Hubei 430074, China

Received 21 March 2019; accepted in revised form 2 October 2019; available online 14 October 2019

Abstract

Melt-rock interaction, a general term describing various processes including cryptic and modal metasomatism and melt-rock reaction, is the main process responsible for modifying chemical composition of previously melt-depleted mantle peridotite. However, the underlying mechanisms of melt-rock interaction and its effect on mantle rheology, particularly in natural peridotites, is poorly constrained. Composite xenoliths are natural examples of melt-rock interaction as they contain pyroxenitic veins interpreted as evidence of passage of melt through peridotite at high pressures. Here, we present new mineral chemistry (major, trace element, and water contents of olivine and pyroxenes) and microstructural data on a suite of composite xenoliths from the Neogene Hannuoba basalt, North China Craton. We show that despite having experienced high melt/rock ratios, olivines and pyroxenes contain very low water contents (<10 ppm and <100 ppm, respectively). In contrast, melts calculated to be in equilibrium with clinopyroxene show enriched trace element signatures suggesting the infiltrating melt had a crustal origin. Microstructural data corroborate a key role for melt infiltration in causing a systematic shift in olivine crystallographic preferred orientation (CPO) from initially A-type to AG-type with increasing melt/rock ratio. By describing the olivine grain shape with respect to the crystal reference frame, we show that as pyroxene mode (and hence melt/rock ratio) increases, olivine grains appear to rotate with their flattest (0 1 0) faces aligning with the melt flow plane, resulting in an olivine CPO controlled by its shape-preferred orientation (SPO). Previously, such an SPO-induced CPO was only demonstrated in shallow magmatic environments such as mafic intrusions, in mafic lavas, and in high-pressure/high-temperature experiments. Such a finding in the deep lithosphere is important as it suggests that dislocation creep may not always play a major role in CPO development, particularly when melt is involved.

Keywords: Composite xenolith; Olivine CPO; Melt-rock reaction

1. INTRODUCTION

Magma generation on Earth occurs primarily within three regimes – mid-ocean ridges, subduction zones, and hotspots, resulting in well-characterized surface expressions: mid-ocean ridge basalts, arc magmas, and ocean island basalts, respectively. However, there may exist a vast, but hidden melt regime in the mantle, which does not manifest as widespread surface volcanism. A number of studies suggest that the seismic low velocity zone beneath oceanic and some continental lithosphere could be the result of a small fraction of partial melt (Schmerr, 2012; Naif et al., 2013; Tharimena et al., 2017). Ubiquitous, but scattered, low-volume intraplate magmas not attributed to deep-seated plumes, such as globally distributed seamounts (Wessel et al., 2010), attest to the presence of

* Corresponding author.
E-mail address: e8chin@ucsd.edu (E.J. Chin).

https://doi.org/10.1016/j.gca.2019.10.002
0016-7037/

sub-lithospheric melts that do manage to erupt. Within continental lithosphere, the enigma of kimberlites may be connected to episodic metasomatism at the base of cratonic lithosphere (Foley, 2008). Infiltration and interaction of low-degree melts with overlying lithosphere can result in pervasive metasomatic and rheological modification of the deep lithosphere (both upper mantle and lower crust) over time (Ionov et al., 2005; Wölbern et al., 2012; Tang et al., 2013). Eventually, such enriched lithosphere may subduct or founder into the deep interior, partially melt, and thus further introduce chemical heterogeneity into the solid earth.

An open question is the extent to which melts modify the overriding lithosphere, and how they may do so. Melt-rock interaction is a general term describing the various processes that may occur during melt transport in the mantle (Zhou et al., 1994; Rampone et al., 2008; Warren, 2016), resulting in compositional, physical, textural, mineralogical, and isotopic modification of peridotite. Collectively, these metasomatic processes can be divided into (1) patent or modal metasomatism, resulting in addition of new, often exotic, minerals (Harte, 1983), (2) stealth metasomatism or refertilization (O'Reilly and Griffin, 2013), which results in re-addition of typical peridotitic minerals, and (3) cryptic metasomatism, resulting in chemical change of minerals (especially with respect to trace elements), but no change in mineral modes (Dawson, 1984). Characterizing the origin and composition of metasomatic agents is important for understanding coupled geodynamic and geochemical processes from a whole-earth perspective. For example, although low-degree, highly fractionated melts derived from mantle melting play an important role in metasomatism (Simon et al., 2003), it is increasingly recognized that tectonic recycling of crustal material also provides potent metasomatic agents, such as subducted carbonate sediments (Liu et al., 2015; Chen et al., 2017). In addition to chemical modification, modal and stealth metasomatism can result in addition of dense phases such as garnet and spinel that crystallize from metasomatic melts; this can have a substantial effect on the densities (Jordan, 1979) and therefore seismic velocities of mantle peridotites (Wagner et al., 2008; Schutt and Lesher, 2010). Moreover, deformation of peridotite in the presence of melt has been shown to modify the crystallographic preferred orientations (CPOs) of the dominant mantle mineral olivine, which has implications for seismic anisotropy (Holtzman et al., 2003; Soustelle and Tommasi, 2010; Higgie and Tommasi, 2012; Baptiste and Tommasi, 2014; Qi et al., 2018).

Despite increasing recognition that presence of melt significantly modifies mantle peridotites, the underlying mechanisms that govern the coupled chemical-physical evolution of peridotite as a result of melt-rock interaction are not well understood. Broadly speaking, the most straightforward type of melt-rock interaction is infiltration of basaltic melt into peridotites. In the shallow mantle (<1.5 GPa), basaltic melts that originally formed at higher pressures dissolve pyroxene and form dunite, because such melts are saturated only in olivine at low pressures (Kelemen et al., 1992). A well-known natural example of this is discordant dunite in ophiolites (Kelemen, 1990). As melt-rock reaction progresses, the melt becomes increasingly richer in orthopyroxene (opx), forming end product harzburgite. With subsequent cooling and crystallization, reacted melts eventually saturate in clinopyroxene (cpx), leading to the formation of lherzolites, websterites, and clinopyroxenites (Kelemen et al., 1992; Mallik and Dasgupta, 2012). During melt-rock reaction at higher pressures, the initial melts of peridotite are more alkali-rich than at lower pressures (Morse, 1980) and the stability field of pyroxene expands relative to that of olivine (Chen and Presnall, 1975). Thus, high pressure melt-rock reaction may result in greater degree of cpx enrichment in the host peridotite (Mallik and Dasgupta, 2012; Tursack and Liang, 2012). Over time, pervasive melt-rock reaction may completely transform large extents of previously depleted peridotite back into fertile lherzolite, in a process known as refertilization (Bodinier and Godard, 2003; Le Roux et al., 2007).

Significant changes in pre-existing microstructure, and therefore rheology, of peridotites may also occur as a result of melt-rock infiltration and reaction. A commonly observed CPO of olivine in natural peridotites is the axial-[0 1 0] or AG-type, where [1 0 0] and [0 0 1] axes show a girdled distribution in the foliation and [0 1 0] axes show point maxima perpendicular to foliation (Ben Ismail and Mainprice, 1998; Bernard et al., 2019). Several hypotheses, with or without melt, have been proposed to explain olivine AG-type CPO. First, the deformation environment itself may be responsible, e.g. transpression (Tommasi et al., 1999; Vauchez et al., 2000) or static recrystallization (Tommasi et al., 2008; Zaffarana et al., 2014; Fernández-Roig et al., 2017). Second, elevated water content in olivine, high pressures, and/or high stress may also promote simultaneous activation of [1 0 0](0 1 0) and [0 0 1](0 1 0) slip systems (Tommasi et al., 2000; Mainprice et al., 2005; Vauchez et al., 2005; Hidas et al., 2007; Bascou et al., 2011; Jung et al., 2014). Third, experimental shearing of peridotite in the presence of melt has been shown to result in development of AG-type olivine CPO (Holtzman et al., 2003; Qi et al., 2018). A number of field and xenolith studies also point to melt infiltration as a cause of the commonly observed AG-type olivine CPO (Dijkstra et al., 2002; Soustelle et al., 2009, 2010; Baptiste and Tommasi, 2014; Higgie and Tommasi, 2014; Chin et al., 2016; Denis et al., 2018). However, the underlying physical-chemical processes responsible for evolution of AG-type CPO remain poorly constrained.

The purpose of this study is to investigate how geochemistry and microstructure evolve in tandem as a result of melt-rock interaction in the deep lithosphere. To this end, we utilize composite mantle xenoliths, which are characterized by both a peridotitic and pyroxenitic component, usually manifested as bands of pyroxenite crosscutting peridotite. The prevailing interpretation of such composite xenoliths is that the pyroxene-rich parts reflect igneous crystallization of basaltic magmas passing through the mantle lithosphere at high pressures (>1 GPa) (Wilshire and Shervais, 1975; Irving, 1980). Thus, composite xenoliths preserve a record of deep lithospheric magmatic processes (Harte et al., 1977; Nielson and Noller, 1987). We analyze a suite of composite xenoliths from the North

China Craton (NCC), an ancient subcontinental lithospheric domain that experienced recent tectonic and magmatic rejuvenation. Our main objectives are to characterize the effects of melt infiltration and refertilization on both the geochemical and microstructural evolution of peridotites by using these composite xenoliths.

2. GEOLOGIC SETTING & SAMPLE SELECTION

2.1. North China Craton lithospheric structure & evolution

The NCC is a major lithospheric terrane in eastern Eurasia preserving crustal rocks older than 3.6 Ga (Liu et al., 1992). The NCC is broadly divided into three regions: the eastern block, the western block, and the trans-North China orogen which records a major collision and suturing of the two blocks between 1.8 and 2.0 Ga (Kusky et al., 2016). During the Late Mesozoic and Cenozoic, the NCC experienced widespread tectonothermal rejuvenation, associated with emplacement and eruption of large volumes of granite and volcanic rocks, respectively (Yang et al., 2003). Geophysical data and thermobarometry of mantle xenoliths erupted in Tertiary volcanic rocks indicate present-day elevated geotherms (60–80 mW/m^2). These xenoliths record relatively high equilibrium temperatures and are generally fertile in composition (Rudnick et al., 2004). In contrast, xenoliths entrained in Ordovician diamond-bearing kimberlites contain garnet and are highly melt-depleted, consistent with the previous presence of a cold, thick cratonic keel (Gao et al., 2002). Geochemical, petrological, and isotopic studies of NCC xenoliths suggest that the Late Mesozoic – Cenozoic tectonothermal event was associated with lithospheric thinning and convective removal of the lower crust (Menzies et al., 1993; Griffin et al., 1998; Gao et al., 2002).

There is systematic variation in crust-mantle structure inferred from xenoliths and seismic refraction data across the NCC. Within the eastern NCC, the depth to the seismic and petrologic Moho coincides at ~30 km, but in the western part of the NCC the petrologic Moho is inferred at ~28 km whereas the seismic Moho at ~42 km, suggesting a thick transitional zone between the crust and mantle boundary (Huang and Xu, 2010). One explanation for the presence of such a crust-mantle transition zone is magmatic underplating during the Late Mesozoic associated with the thermal reactivation of the NCC (Wilde et al., 2003).

The Hannuoba basalt field (14–27 Ma; Zhu (1998)), located at the northern margin of the trans-North China orogen, contains abundant lower crustal (granulite) and upper mantle (peridotite and pyroxenite) xenoliths. Both xenolith types, particularly those sampled from the Damaping locality (40°58′ N, 114°31′ E), have been the subject of numerous previous studies (Xu, 2002; Liu et al., 2003, 2004; Rudnick et al., 2004; Liu et al., 2010). Coupled petrological and geochemical studies of the granulites and mantle xenoliths suggest that the two are genetically linked: melt-rock reaction within the uppermost mantle with a silicic melt resulted in composite pyroxenite-bearing peridotite, and subsequent formation of the granulites by crystallization of melts derived from the melt-peridotite interaction (Liu et al., 2005). Furthermore, U-Pb zircon ages of the Hannuoba xenoliths show zircons containing Precambrian cores but with Mesozoic overgrowth rims, consistent with an overprint due to basaltic underplating and subsequent granulite-facies metamorphism at ~160–80 Ma (Liu et al., 2004). Thus, both lower crustal and upper mantle xenoliths from Damaping record recent magmatic processes in the deep lithosphere.

2.2. Sample selection & rationale

We selected 6 composite xenoliths (DMP-441, DMP-314, DMP-124, DMP-448, DMP-464, DMP-315; shown in Fig. 1) from Damaping that were previously analyzed for petrology and whole-rock geochemistry by Liu et al. (2005). One xenolith, DMP-315, was also previously analyzed by Liu et al. (2004) for Sr-Nd-Pb isotopes and U-Pb zircon ages. All of the selected xenoliths were previously interpreted by Liu et al. (2005) to have experienced some degree of melt-rock interaction. On the basis of petrography, Liu et al. (2005) divided the composite xenoliths into Type I and Type II; the former are clinopyroxene-rich spinel pyroxenites and are thought to represent magmatic cumulates, whereas the latter are garnet pyroxenite veins hosted in spinel lherzolites, and are thought to represent products of melt-rock reaction. Of the 6 selected xenoliths in this study, 2 fall under the Type I category (DMP-314, DMP-315) and 4 fall under the Type II category (DMP-124, DMP-448, DMP-464, DMP-440). The reader is referred to Liu et al. (2005) for optical images and photomicrographs of the xenoliths.

Of the 6 xenoliths we selected from Liu et al. (2005) for this study, we performed full-thin section EBSD maps for all, and then selected 3 (DMP-314, DMP-124, DMP-315) for detailed mineral chemistry and H_2O analyses (Fig. 1) (see Section 3). All new analytical work was done on existing thin sections and/or the associated billets of those thin sections (e.g., for mineral separation). This approach ensures that mineral chemistries and H_2O contents analyzed on mineral separates reflect as close as possible the textures analyzed in corresponding thin sections. In selecting the xenoliths, our rationale was to encompass the full spectrum of textural variation from peridotitic wallrock (e.g., DMP-441, DMP-314) to xenoliths with preserved contacts with pyroxenite veins (DMP-124, DMP-448, DMP-464), to xenoliths representative of mostly the pyroxenite vein itself (DMP-315).

3. METHODS

3.1. Phase & crystal orientation mapping: Electron Backscatter Diffraction (EBSD)

Fully automated EBSD maps of entire thin sections of the studied xenoliths were collected on an FEI Quanta 450 SEM at the State Key Laboratory of Geological Processes and Mineral Resources, China University of Geosciences (Wuhan). Selected thin sections were also mapped using the FEI Apreo LoVac field-emission SEM with an Oxford Symmetry EBSD detector at UC San

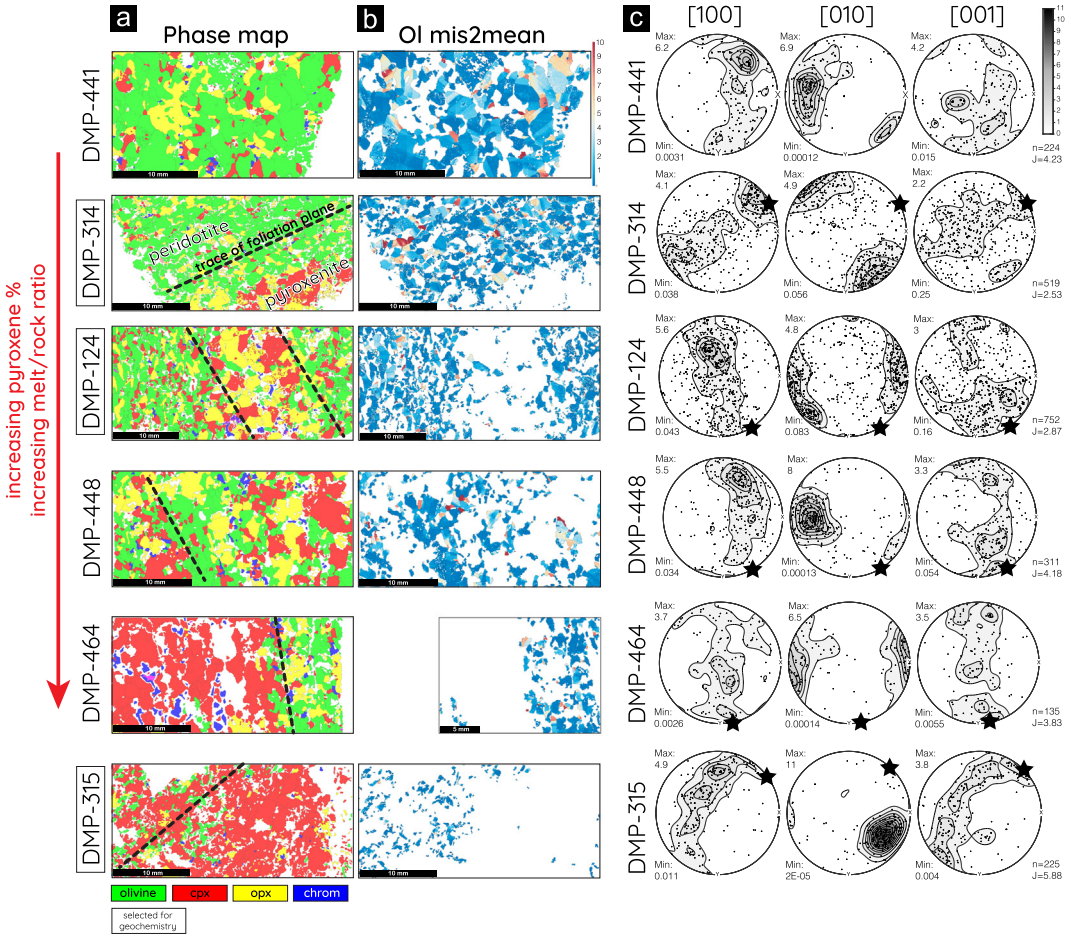

Fig. 1. EBSD maps of DMP composite peridotite-pyroxenite xenoliths. (A) Phase maps. Dashed black lines show the trace of the foliation plane. (B) Olivine mis2mean maps. (C) Olivine CPOs plotted as pole figures (lower hemisphere, equal-area projection, contours at one half multiple of uniform distribution, n = number of grains, J = J index). Black stars mark the apparent lineation (inferred from the trace of the foliation plane).

Diego. Prior to analyses thin sections were polished by hand and on lap wheels for several hours with a 0.05 μm colloidal alumina suspension. The specimen was tilted 70° in the sample chamber and EBSD measurements were carried out at an accelerating voltage of 20 kV; a beam current of 2.4 nA at a working distance of 24–25 mm; and spot size of 6 μm. Diffraction patterns were collected using Channel 5 software from Oxford Instruments HKL technology. Measurements with a mean angular deviation (MAD) > 1° were discarded. The indexing rates were between 65 to 90%. The maps were then processed through a cleaning routine in Oxford Instruments Channel5 software Flamenco to first remove wild spikes, then filling of crystal orientations of non-indexed pixels down to 5 nearest neighbors, and finally correction for olivine pseudosymmetry (60° around [1 0 0]). The EBSD maps were further processed in MTEX 5.1.1, an open source Matlab toolbox (Hielscher and Schaeben, 2008; Bachmann et al., 2011; Mainprice et al., 2015) (http://mtex.googlecode.com). It was used for analysis and modeling of crystallographic textures, including plotting of orientation maps, and CPOs. A "de la Vallée Poussin" kernel with a half-width of 10° was used for the calculation of orientation distribution functions for olivine and orthopyroxene. Grains were constructed in MTEX using a critical misorientation of 10°, and orientation distribution functions (one point per grain, Gaussian half width of 10°) for olivine, cpx, and opx were calculated and used to contour the CPO data and calculate the J-index (Bunge, 1982).

3.2. Mineral chemistry: SIMS, EPMA, and LA ICP-MS

To facilitate as consistent of a comparison as possible between the areas mapped by EBSD and mineral compositional analysis, we took the original billets of the thin sections and sub-sampled them for mineral separates. High-purity olivine, cpx, and opx grains were handpicked using a binocular microscope following gentle hand crushing of ~5 cm sections of each xenolith billet. Grains with visible cracks, alteration, and inclusions were discarded. The mineral grains, together with a piece of commercially available Suprasil glass (H_2O content ~1 ppm; used for background monitoring during secondary ion mass spectrometry analysis (SIMS)) were then mounted in aluminum disks filled with indium, pressed, ground with alumina sandpaper and polished with diamond compounds down to 0.25 μm.

All subsequent geochemical analyses (SIMS, EPMA, LA-ICPMS, in sequence) were done on the indium mounts.

Olivine and pyroxenes were then analyzed for water concentrations using a CAMECA 7f-Geo SIMS at the Caltech Microanalysis Center, following protocols described in detail in Chin et al. (2016), which we summarize here. The ion microprobe was first "baked" for 48 h to reach ultra high vacuum ($\sim 2 \times 10^{-10}$ torr), samples and standards were placed into the airlock ($\sim 5 \times 10^{-9}$ torr) for at least 48 h prior to measurement. Analyses were made using a primary Cs^+ beam with current of 4.5–5 nA and accelerating voltage of 10 kV. We rastered the primary beam over a 20 × 20 μm area and collected secondary ions from an 8 μm spot in the center of the rastered area, limited with a field aperture. For each analysis, 2 min of presputtering was followed by 30 cycles through the mass sequence ^{12}C, $^{16}O^1H$, ^{18}O, ^{19}F, ^{27}Al, and ^{30}Si. A mass resolving power ~5200 was used to separate $^{16}O^1H$ from ^{17}O. We measured standards from Aubaud et al. (2007), Mosenfelder et al. (2011), and Mosenfelder and Rossman (2013a,b) and used these to construct matrix-matched calibration curves for each mineral. The Suprasil glass was routinely analyzed to monitor background water contents (~1 ppm). Analytical uncertainties ranged from 10 to 15% (2 RSE).

Following SIMS work, olivines and pyroxenes were analyzed for major elements using the CAMECA SX100 electron microprobe at Brown University (15 kV, 20 nA beam current, 1 μm spot size); standards used for calibration were Wakefield diopside (Si, Ca), synthetic rutile (Ti), Kakanui hornblende (Al), synthetic $MgCr_2O_4$ (Cr), Rockport fayalite (Fe), rhodonite (Mn), synthetic forsterite (Mg), and Amelia albite (Na). We also used the following secondary standards: Lunar Crater augite, San Carlos olivine, and Natural Bridge diopside. Relative standard deviations were <1% for major elements and 3–5% for minor elements. Care was taken to select spots as close as possible to previous ion microprobe pits. Lastly, trace element compositions of pyroxenes were analyzed by laser ablation (LA) ICP-MS using a 193 nm wavelength excimer Analyte G2 laser coupled to a Thermo Scientific X-Series II ICP-MS at Brown University. Laser spots (65 μm for cpx, 85 μm for opx) were selected to be as close as possible to the EPMA and SIMS spots. The laser was run at a fluence of 3.78 J/cm^2 at 50% energy at 10 Hz. At the start of the session, the ICP-MS was tuned on a 65 μm spot on a line transect using NIST 612 glass to achieve sensitivy of ≥90,000 cps per 35 ppm La. External standards used were the USGS glass standards BHVO2-G, BIR1-G, and BCR2-G; ^{26}Mg was used as the internal standard. Analytical precision ranged from 10 to 15 % (RSD) on average for elements with concentrations >10 ppm and 20–30% (RSD) for elements with concentrations <1 ppm.

4. RESULTS

4.1. Major, trace element, and H_2O concentration in nominally anhydrous minerals

Major element, trace element, and H_2O concentration data are reported in Tables 1 and 2 for olivine and pyroxenes, respectively. In general, major element, trace element, and H_2O concentrations of mineral cores and rims were similar within individual xenoliths (with the exception of zoned opx in one sample, discussed below), but varied across different xenoliths. For a given xenolith, mineral separates from the same billets originally used for the thin sections also showed similar compositions regardless of whether they originated from vein or host. We interpret this to reflect chemical equilibrium across vein-host rock contacts at the individual xenolith scale.

4.1.1. Olivine

Major element, selected minor element, and H_2O concentrations of olivine are reported in Table 1. Olivines are homogeneous with no resolvable zoning in major, trace, or H_2O content. In all three xenoliths analyzed, there is a systematic decrease in Mg# (atomic Mg/Mg + Fe) with increasing clinopyroxene mode, ranging from Mg# = 91 in DMP-314, Mg# = 88 in DMP-124, and Mg# = 82 in DMP-315 (Fig. 2a). Furthermore, olivine H_2O contents also increase from 4.8 (±0.4 2σ) ppm in DMP-314, the most cpx-poor xenolith, to 6.7 (±0.7 2σ) in DMP-124, to 9.1 (±1.7 2σ) in DMP-315, the most cpx-rich xenolith (Fig. 2a). Within Type I ("cumulate") xenoliths, NiO decreases from 0.4 wt.% (±0.16 wt% 2σ) in DMP-314 to 0.12 (±0.07 wt% 2σ) in DMP-315 as H_2O increases, whereas Ti increases from ~10 to ~20 ppm in DMP-314 and DMP-315, respectively (Fig. 2b). Interestingly, DMP-124, the Type II ("melt-rock reacted") xenolith falls off of these H_2O vs. NiO, Ti trends, plotting at higher Ti and intermediate H_2O but similar NiO to the cpx-poor DMP-314 (Fig. 2b). An explanation for these trends corroborates the Type I vs. Type II classification originally proposed by Liu et al. (2005) – Type I cumulates should represent near-instantaneous fractionally crystallized assemblages from mafic melts (Xu, 2002), and thus should show large variations in Mg# and trace element content, whereas Type II pyroxenite veins would have their Mg#'s (and NiO) contents buffered by peridotite (Liu et al., 2005). Note that these chemical trends interpreted by Liu et al. (2005) were generalized for the spectrum of bulk rock compositions observed, and so correspond to a spatial scale (i.e. hand samples) larger than the individual thin section scales investigated here.

4.1.2. Opx

Orthopyroxene (opx) major element, trace element, and H_2O contents are reported in Table 2. Like olivine, opx are homogeneous with respect to major elements. Opx are aluminous enstatites (>3 wt.% Al_2O_3; Table 2). The high aluminum content is characteristic of pyroxene found in cumulate-type xenoliths (Irving, 1974; Best, 1975; Sen, 1988). The Mg# of opx is slightly higher than that of olivine, due to K_D Fe-Mg ~ 1 (von Seckendorff and O'Neill, 1993).

Water concentration of opx in all xenoliths are below 100 ppm H_2O (Fig. 3). The most opx-poor xenolith (but most cpx-rich), DMP-315, has higher H_2O in cores than in rims (Δcore-rim = 24 ppm); this degree of zoning is above analytical uncertainty of the SIMS measurement.

Table 1
Olivine major element composition and H_2O contents.

	DMP-315	DMP-315	DMP-315	DMP-315	DMP-315	DMP-314	DMP-314	DMP-314	DMP-314	DMP-314	DMP-124	DMP-124	DMP-124	DMP-124	DMP-124	DMP-124
	OLIVINE	OLIVINE	OLIVINE	OLIVINE	OLIVINE	OLIVINE	OLIVINE	OLIVINE	OLIVINE	OLIVINE	OLIVINE	OLIVINE	OLIVINE	OLIVINE	OLIVINE	OLIVINE
	MT1_02OLC	MT1_02OLR	MT1_03OLC	MT1_03OLR	MT1_07OLC	MT1_07OLR	MT1_34OLC	MT1_34OLR	MT1_35OLC	MT1_35OLR	MT1_33OLR	MT2_5OLC	MT2_5OLR	MT2_3OLC	MT2_3OLR	MT2_4OLC	MT2_4OLR
wt.%	core	rim	core	rim	core	rim	core	rim	core	rim	rim	core	rim	core	rim	core	rim
SiO_2	39.33	39.61	39.41	39.78	39.43	39.61	41.31	41.16	41.22	41.07	40.98	41.04	40.9	40.39	40.82	41.11	41.04
TiO_2	0.01	0.01	bdl	bdl	bdl	bdl	bdl	0.01	bdl	bdl	0.01	bdl	0.01	0.01	0.01	bdl	0.01
Al_2O_3	bdl	0.01	bdl	bdl	bdl	0.01	bdl	bdl	bdl	bdl	bdl	0.01	0.01	0.02	0.02	0.02	0.01
Cr_2O_3	0.01	bdl	bdl	bdl	0.03	bdl	bdl	bdl	0.02	0.01	0.01	bdl	0.01	bdl	0.01	0.01	0.01
FeO	17.47	17.11	17.49	17.33	17.8	17.42	9.41	9.33	9.21	9.3	9.59	11.53	11.74	12.11	11.66	11.92	11.75
MnO	0.24	0.22	0.23	0.22	0.25	0.25	0.18	0.13	0.14	0.14	0.12	0.18	0.15	0.19	0.15	0.13	0.17
MgO	43.37	43.39	43.41	43.61	43.57	43.63	50.01	49.92	49.97	49.81	50.02	47.28	47.17	47.79	47.67	47.31	47.69
CaO	0.04	0.03	0.03	0.03	0.03	0.03	0.02	0.03	0.03	0.02	0.02	0.06	0.07	0.07	0.06	0.05	0.06
Na_2O	bdl	bdl	0.02	0.01	bdl	0.03	0.01	0.01	0.02	bdl	0.02	bdl	bdl	0.02	0.02	bdl	bdl
NiO	0.11	0.12	0.07	0.16	0.11	0.16	0.35	0.49	0.32	0.38	0.35	0.28	0.42	0.44	0.28	0.49	0.4
Total	100.57	100.49	100.65	101.15	101.24	101.14	101.29	101.07	100.93	100.75	101.11	100.38	100.46	101.05	100.7	101.05	101.14
Mg#	81.6	81.9	81.6	81.8	81.4	81.7	90.5	90.5	90.6	90.5	90.3	88.0	87.8	87.6	87.9	87.6	87.9
ppm																	
H_2O	7.8	9.1	8.9	8.8	10.1	9.9	5.1	4.6	4.8	4.7	4.8	6.4	6.4	6.8	6.9	6.4	7.1

DMP-124 and DMP-314 both show higher H_2O cores than rims, but the Δcore-rim falls within the range of analytical uncertainty.

4.1.3. Cpx

Clinopyroxene (cpx) major element, trace element, and H_2O contents are reported in Table 2. Similar to olivine and opx, cpx are also homogeneous with respect to major elements. Cpx are chromian diopside (~0.5 to ~1 wt.% Cr_2O_3). The Mg# of cpx is slightly greater than that of olivine and opx, due to K_D Fe-Mg between cpx and olivine being greater than 1 (Pearson et al., 2003). Na_2O content is variable, ranging from 0.6 wt.% in DMP-315, 1.4 wt.% in DMP-314, and 2.2 wt.% in DMP-124. Al_2O_3 follows Na_2O, with Al_2O_3 ranging from 4.5, 5, and 7.7 wt.% in DMP-315, DMP-314, and DMP-124, respectively.

Primitive-mantle normalized incompatible trace element concentrations in cpx are plotted in Fig. 4. Trace element patterns are similar between Type I xenoliths DMP-314 and DMP-315, with DMP-315 having higher overall trace element abundances than DMP-314. Both DMP-314 and DMP-315 exhibit highly fractionated cpx patterns characterized by very low Rb and Ba and depletion in Nb, Ta, Zr, Hf (high-field strength elements, or HFSE) relative to large ion lithophile elements (LILE). In contrast, Type II xenolith DMP-124 lacks a negative Nb, Ta and Zr, Hf anomaly, but also shows extremely low Rb and Ba abundances similar to Type I xenoliths.

H_2O concentration in cpx are similar to those in opx, with all cpx having <100 ppm H_2O. There is a positive correlation with cpx mode and cpx H_2O concentration (Fig. 3a), with H_2O concentration increasing from ~50 ppm in DMP-314 to ~80 ppm in DMP-315. H_2O content in cpx cores and rims are the same within analytical uncertainties (Fig. 3c).

4.2. Textural characteristics of composite xenoliths

Fig. 1a presents EBSD phase maps processed in MTEX. We show maps of the 6 selected composite xenoliths, ranked from pyroxene-poor, peridotitic (DMP-441, Type II), to peridotite with a small pyroxenite vein in sharp contact (DMP-314, Type I), to increasingly pyroxene-rich, as shown by the 3 xenoliths with pyroxenite veins hosted in lherzolite (DMP-124, DMP-448, DMP-464, Type II), and finally to a xenolith that is nearly all pyroxenite vein (DMP-315, Type I). Garnet is present in DMP-124, DMP-448, and DMP-464, but owing to extensive decomposition and kelyphitization (Liu et al., 2005) it was not possible to index garnet using EBSD, and so garnet appears as blank areas in the EBSD phase maps.

From the quantitative EBSD phase maps in Fig. 1a, we can draw several observations about various mineral-mineral relationships and textures. In the most peridotitic xenolith (DMP-441), the olivines are coarse-grained and show curvilinear grain boundaries with a few scattered triple junctions; the pyroxenes are characterized by interlobate phase boundaries with some smaller grains appearing within interstices between olivines. The increasingly veined xenoliths show both a decrease in olivine grain

Table 2
Pyroxene major element, trace element, and H_2O contents.

	DMP-124	DMP-124	DMP-124	DMP-124	DMP-124	DMP-124	DMP-314	DMP-314	DMP-314	DMP-314	DMP-314	DMP-314	DMP-314	DMP-315	DMP-315
	OPX	OPX	OPX	OPX	OPX	OPX	OPX	OPX	OPX	OPX	OPX	OPX	OPX	OPX	OPX
	07-Mt2-8OPc	08-Mt2-8Opr	18-Mt2_7Op_r	7Op core	19-Mt2_6Op_c	20-Mt2_6Op_r	32-Mt1_28Op_c	33-Mt1_28Op_r	34-Mt1_27Op_c	35-Mt1_27Op_r	43-Mt1_31Op_r	65_Mt1_32opx_c	66_mt1_32opx_r	44-Mt1_16Op_c	45-Mt1_16Op_r
wt.%	core	rim	rim	core	core	rim	core	rim	core	rim	rim	core	rim	core	rim
SiO_2	54.9	54.84	54.26	54.37	54.85	54.67	56.15	56.17	56.03	56.39	56.67	56.34	56.47	53.98	54.16
TiO_2	0.16	0.15	0.16	0.16	0.17	0.17	0.07	0.08	0.09	0.08	0.07	0.08	0.08	0.16	0.13
Al_2O_3	4.93	5.04	5.1	5.06	5.21	5.09	3.61	3.4	3.37	3.17	3.07	3.34	3.16	3.63	3.34
Cr_2O_3	0.22	0.24	0.24	0.23	0.24	0.23	0.47	0.4	0.46	0.43	0.41	0.49	0.42	0.3	0.19
FeO_T	7.25	7.25	7.41	7.39	7.27	7.57	5.86	5.94	6.07	6.07	6.14	5.98	5.87	11.16	11.18
MnO	0.18	0.17	0.14	0.14	0.16	0.15	0.14	0.14	0.14	0.17	0.14	0.18	0.11	0.25	0.26
MgO	31.51	31.72	31.76	31.78	32.24	32.07	33.7	34.24	34.1	34.18	34.39	34.11	34.06	30.24	30.34
CaO	0.67	0.68	0.76	0.72	0.65	0.71	0.51	0.44	0.5	0.46	0.42	0.53	0.44	0.49	0.46
Na_2O	0.13	0.2	0.13	0.19	0.16	0.15	0.06	0.01	0.04	0.07	0.02	0.02	0.02	0	0.02
NiO	0.15	0.12	0.15	0.1	0.18	0.12	0.05	0.09	0.08	0.06	0.08	0.01	0.02	0.04	0.01
Total	100.1	100.42	100.12	100.15	101.13	100.95	100.61	100.91	100.87	101.08	101.42	101.08	100.65	100.24	100.08
Mg#	88.6	88.6	88.4	88.5	88.8	88.3	91.1	91.1	90.9	90.9	90.9	91.0	91.2	82.9	82.9
ppm															
Cs	bdl	bdl	bdl		0.003	0.008	0.001	0.004	0.005	0.003	0.025	bdl	0.0007	0.003	0.223
Pb	bdl	0.001	0.012		0.004	0.008	0.001	bdl	bdl	0.008	0.011	0.031	0.037	0.004	bdl
U	0.0008	0.0004	bdl		0.0005	0.0004	bdl	0.0004	bdl	bdl	0.0004	0.0005	0.0017	0.0012	0.0004
Th	0.0005	bdl	bdl		bdl	bdl	bdl	bdl	bdl	0.0005	0.0005	0.0006	0.002	0.007	0.001
Li	9.41	10.5	4.42		10.9	7.70	0.74	0.32	2.63	1.55	0.44	3.21	3.67	1.64	1.94
Ba	bdl	0.005	0.010		0.006	0.005	bdl	0.005	bdl	bdl	0.063	0.006	bdl	0.027	bdl
Rb	0.006	bdl	0.006		0.005	bdl	bdl	0.006	bdl	bdl	0.004	bdl	bdl	0.0008	bdl
Nb	0.005	0.005	0.014		0.007	0.012	0.006	0.01	0.009	0.003	0.003	0.008	0.006	0.004	0.008
Ta	bdl	0.0005	0.0004		0.001	0.001	bdl	bdl	0.0005	bdl	bdl	0.0006	bdl	bdl	bdl
La	0.0007	0.001	0.001		0.002	0.001	bdl	0.0007	0.0007	bdl	bdl	0.002	0.004	0.010	0.004
Ce	0.010	0.016	0.016		0.009	0.013	0.006	0.006	0.006	0.003	0.005	0.010	0.025	0.038	0.015
Pr	0.003	0.003	0.004		0.005	0.001	0.002	0.0005	0.001	0.0006	0.001	0.001	0.002	0.005	0.003
Sr	0.149	0.137	0.180		0.127	0.151	0.070	0.065	0.072	0.061	0.046	0.084	0.113	0.224	0.081
Nd	0.018	0.009	0.020		0.033	0.024	0.003	0.013	0.003	0.009	0.015	0.011	0.018	0.035	0.036
Zr	1.89	1.76	2.06		2.05	1.93	0.630	0.494	0.585	0.519	0.431	0.615	0.580	1.27	1.29
Hf	0.049	0.057	0.065		0.060	0.055	0.026	0.016	0.025	0.022	0.019	0.023	0.022	0.056	0.055
Sm	0.026	0.007	0.031		0.015	0.044	0.011	0.004	0.004	0.011	0.014	0.016	0.021	0.036	0.013
Eu	0.013	0.014	0.014		0.011	0.010	0.003	0.003	0.0009	0.005	0.0009	bdl	0.003	0.016	0.010
Ti	859	852	883		858	870	425	397	419	391	382	414	424	886	802
Gd	0.065	0.070	0.084		0.080	0.060	0.020	0.016	0.027	0.023	0.015	0.013	0.022	0.045	0.054
Tb	0.016	0.015	0.017		0.015	0.019	0.0036	0.0058	0.0063	0.0037	0.0041	0.0048	0.011	0.012	0.011
Dy	0.148	0.125	0.142		0.134	0.138	0.040	0.052	0.050	0.049	0.039	0.066	0.066	0.110	0.115
Ho	0.038	0.041	0.040		0.044	0.049	0.017	0.011	0.014	0.007	0.014	0.016	0.015	0.030	0.028
Er	0.115	0.146	0.163		0.124	0.132	0.067	0.063	0.050	0.056	0.056	0.081	0.066	0.096	0.102
Tm	0.025	0.020	0.030		0.023	0.030	0.015	0.016	0.012	0.013	0.010	0.014	0.018	0.014	0.021
Yb	0.191	0.160	0.261		0.260	0.249	0.138	0.099	0.154	0.099	0.098	0.179	0.165	0.174	0.146
Lu	0.036	0.035	0.045		0.041	0.041	0.024	0.020	0.023	0.025	0.022	0.028	0.032	0.031	0.031
Cu	2.16	2.06	1.42		2.30	1.08	0.581	0.327	0.901	0.740	0.305	1.18	1.07	0.2234	0.2453
Sc	13.4	14.0	15.4		14.5	14.3	16.2	15.6	16.2	15.6	14.9	17.0	17.0	24.6	23.8
Zn	36.8	34.8	36.8		37.8	37.2	25.4	26.0	26.6	27.0	26.8	29.0	28.9	69.1	68.4
Co	58.7	59.1	61.6		62.5	61.2	53.0	52.5	53.6	54.8	53.5	57.5	57.2	70.0	70.9
Cr	1404	1399	1616		1573	1529	3086	2819	2965	2799	2565	3484	3436	1643	1545
Ni	636	643	655		681	670	578	577	591	601	586	629	621	183	186
ppm															
H_2O	34.7	30.6	35.0	42.6	40.5	29	24.1	25	31.5	27.8	25.1	26.6	27.7	81.9	56.6

Table 2 (*continued*)

	DMP-315	DMP-315	DMP-315	DMP-315	DMP-124	DMP-124	DMP-124	DMP-124	DMP-124	DMP-124	DMP-314	DMP-314	DMP-314	DMP-314
	OPX	OPX	OPX	OPX	CPX	CPX	CPX	CPX	CPX	CPX	CPX	CPX	CPX	CPX
	46-Mt1_15Op_c	47-Mt1_15Op_r	48-Mt1_14Op_c	49-Mt1_14Op_r	11-Mt2_9Cp_c	12-Mt2_9Cp_r	13-Mt2_11Cp_c	14-Mt2_11Cp_r	15-Mt2_10Cp_c	16-Mt2_10Cp_r	25-Mt1_24CP_c	27-Mt1_25Cp_c	28-Mt1_25Cp_r	29-Mt1_24Cp_r119
wt.%	core	rim	core	rim	core	rim	core	rim	core	rim	core	core	rim	rim
SiO_2	53.86	54.36	54.52	54.2	52.31	52.31	51.52	51.84	52.06	52.19	52.92	52.92	52.75	52.84
TiO_2	0.14	0.12	0.16	0.12	0.77	0.75	0.76	0.72	0.75	0.74	0.24	0.29	0.28	0.27
Al_2O_3	3.31	3.2	3.55	3.43	7.62	7.65	7.83	7.65	7.6	7.74	5.09	4.96	4.65	5.08
Cr_2O_3	0.21	0.19	0.25	0.26	0.51	0.51	0.52	0.47	0.57	0.58	1.24	1.37	1.16	1.28
FeO_T	11.24	11.65	11.32	11.33	3.4	3.4	3.48	3.52	3.44	3.39	2.47	2.31	2.33	2.29
MnO	0.2	0.25	0.24	0.24	0.11	0.1	0.1	0.1	0.08	0.07	0.09	0.08	0.09	0.08
MgO	30.51	30.61	30.31	30.38	14.77	14.85	14.64	14.51	14.6	14.65	15.58	15.54	15.81	15.55
CaO	0.41	0.43	0.51	0.43	18.93	18.91	19.23	18.68	18.9	18.94	21.77	21.88	22.08	21.73
Na_2O	0.05	bdl	bdl	bdl	2.18	2.2	2.27	2.28	2.11	2.12	1.55	1.39	1.35	1.44
NiO	0.08	0.04	0.04	0.06	0.04	0.04	bdl	0.07	0.07	0.03	0.03	0.07	0.05	0.04
Total	100.02	100.86	100.9	100.43	100.64	100.72	100.34	99.84	100.18	100.43	100.98	100.81	100.54	100.6
Mg#	82.9	82.4	82.7	82.7	88.6	88.6	88.2	88.0	88.3	88.5	91.8	92.3	92.4	92.4
ppm														
Cs	bdl	0.0007	0.0046	0.0006	0.177	0.003	0.0007	0.001	0.0007	0.003	0.005	0.0006	bdl	bdl
Pb	0.003	0.005	0.006	0.012	0.026	0.038	0.032	0.049	0.029	0.058	0.073	0.078	0.072	0.118
U	0.0007	bdl	bdl	bdl	0.0073	0.0059	0.0135	0.0089	0.0078	0.0078	0.0278	0.0295	0.0227	0.0353
Th	0.001	0.0005	bdl	0.006	0.028	0.030	0.025	0.026	0.031	0.032	0.146	0.144	0.135	0.152
Li	1.41	1.58	1.95	2.26	11.9	11.7	9.8	17.0	10.6	12.8	1.75	2.88	2.95	2.79
Ba	0.010	bdl	bdl	bdl	0.071	0.062	0.016	0.042	0.025	0.039	0.008	bdl	0.024	0.009
Rb	bdl	0.009	0.006	0.002	bdl	0.004	0.009	0.007	bdl	0.007	0.001	bdl	0.005	0.005
Nb	0.005	0.003	bdl	0.001	0.340	0.350	0.355	0.324	0.383	0.387	0.357	0.330	0.314	0.391
Ta	0.002	bdl	bdl	0.0005	0.032	0.032	0.035	0.037	0.038	0.027	0.018	0.018	0.020	0.018
La	0.002	0.001	0.002	0.001	1.12	1.21	1.14	1.11	1.16	1.16	2.27	2.18	2.06	2.33
Ce	0.010	0.004	0.009	0.013	4.30	4.51	4.49	4.38	4.41	4.58	7.14	7.15	6.74	7.51
Pr	0.0005	0.003	0.002	0.002	0.836	0.871	0.884	0.832	0.883	0.913	1.14	1.20	1.09	1.26
Sr	0.037	0.033	0.051	0.039	71.1	73.4	70.1	70.1	70.9	72.8	77.3	75.8	73.6	81.3
Nd	0.014	0.019	0.019	0.029	5.32	5.27	5.23	5.26	5.20	5.41	5.95	6.12	5.86	6.37
Zr	0.934	0.974	1.06	1.11	42.8	46.0	43.3	42.3	44.0	44.3	13.8	14.5	14.6	14.8
Hf	0.045	0.031	0.032	0.052	1.36	1.45	1.35	1.33	1.33	1.37	0.477	0.513	0.520	0.541
Sm	0.025	0.014	0.011	0.007	2.15	2.18	2.02	1.95	2.01	2.19	1.38	1.55	1.45	1.61
Eu	0.003	0.007	0.006	0.005	0.811	0.869	0.870	0.846	0.878	0.877	0.473	0.492	0.478	0.502
Ti	655	651	700	706	4103	4247	4157	3948	4104	4067	1371	1474	1467	1441
Gd	0.061	0.031	0.030	0.048	3.30	3.20	3.45	3.33	3.55	3.66	1.58	1.71	1.57	1.85
Tb	0.012	0.013	0.015	0.014	0.524	0.627	0.603	0.626	0.614	0.616	0.251	0.265	0.285	0.285
Dy	0.096	0.076	0.092	0.082	3.50	3.77	4.12	3.85	4.03	4.29	1.58	1.74	1.64	1.73
Ho	0.019	0.014	0.023	0.021	0.759	0.761	0.902	0.808	0.885	0.869	0.336	0.358	0.353	0.360
Er	0.065	0.096	0.118	0.071	1.94	1.92	2.33	2.17	2.38	2.31	0.888	1.05	0.991	1.04
Tm	0.013	0.016	0.019	0.021	0.252	0.264	0.312	0.294	0.319	0.339	0.129	0.148	0.137	0.147
Yb	0.120	0.139	0.183	0.164	1.56	1.58	2.26	1.94	2.11	2.05	0.857	0.978	0.949	1.01
Lu	0.029	0.035	0.019	0.033	0.198	0.221	0.302	0.286	0.301	0.300	0.128	0.144	0.139	0.144
Cu	0.2348	0.1418	0.2931	0.2479	2.44	2.31	2.03	2.72	1.00	11.6	0.628	0.754	1.79	1.47
Sc	22.7	23.3	23.3	24.0	53.6	56.3	56.5	53.1	57.2	56.8	52.7	57.9	63.1	58.8
Zn	68.5	71.8	69.1	70.3	9.82	9.43	9.29	9.62	10.1	10.2	4.66	4.79	5.23	4.85
Co	69.9	71.1	71.0	71.3	21.8	22.1	21.1	21.6	21.9	22.2	16.1	16.3	16.2	17.6
Cr	1365	1263	1749	1622	3175	3214	3409	3161	3606	3555	7420	8098	6889	8068
Ni	185	188	190	190	289	298	290	288	293	304	257	249	246	265
ppm														
H_2O	87.4	69.8	84.5	55	60.7	59.6	62.1	61.9	63.6	66.6	47	48.7	47.4	49.3

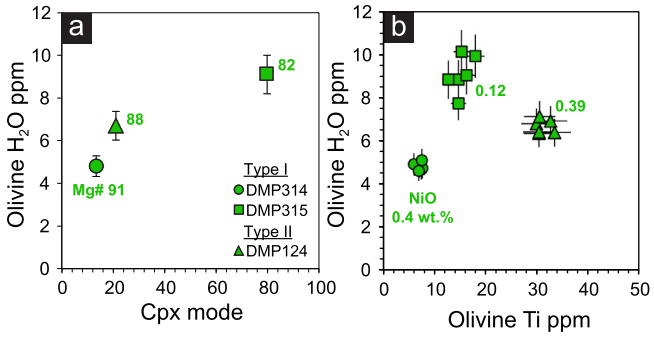

Fig. 2. (a) Olivine H_2O vs. cpx mode, (b) olivine H_2O vs. olivine Ti concentration.

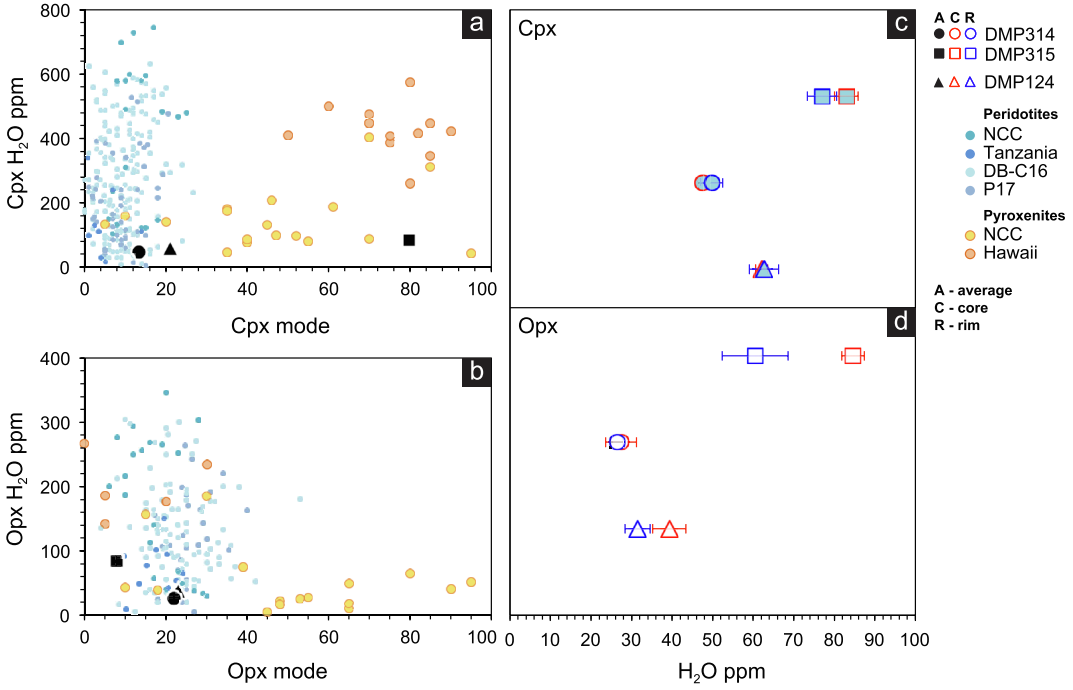

Fig. 3. Pyroxene H_2O systematics. (a) Cpx H_2O vs. Cpx mode; (b) Opx H_2O vs. Opx mode. Peridotite data from the following sources: NCC (Li et al., 2015), Tanzania (Hui et al. (2015)), global compilations (DBC16) and P17 from Demouchy and Bolfan-Casanova (2016) and Peslier et al. (2017), respectively. Pyroxenite data for NCC from Hao et al. (2018) and for Hawaii from Bizimis and Peslier (2015). (c) Core and rim cpx H_2O for the studied xenoliths, (d) core and rim opx H_2O for the studied xenoliths.

size and an increase in the amount of cpx and opx, particularly in the all-pyroxenite xenolith DMP-315 where the olivine grain size is much smaller compared to the other xenoliths. Except for DMP-464, a protogranular peridotite and DMP-314, which has a sharp contact between pyroxenite and peridotite, the other veined xenoliths show gradational contacts from the pyroxenite vein into the peridotite host. Another observation associated with increasing modal pyroxene is that olivines in the veined xenoliths, at least qualitatively, appear to form more tablet-shaped grains, in contrast to the typical protogranular texture of the pyroxenite-poor xenoliths DMP-314 and DMP-441. Finally, the number of olivines with subgrain boundaries, which testify to deformation under the dislocation creep regime, decreases as pyroxene modal abundance increases (Fig. 1b, mis2mean map, discussed in detail in a later section).

4.3. Microstructural observations

4.3.1. Olivine deformation microstructures and CPO

Large area EBSD map data are presented for the 6 selected xenoliths in Fig. 1a and b. Olivine CPOs are shown in Fig. 1c. Although here we show the data for the entire thin sections, we also processed the EBSD map data to separate out peridotitic and pyroxenitic areas of the xenoliths (SI Fig. 1). We found that the olivine CPOs were similar in both peridotitic and pyroxenitic areas; with the strength

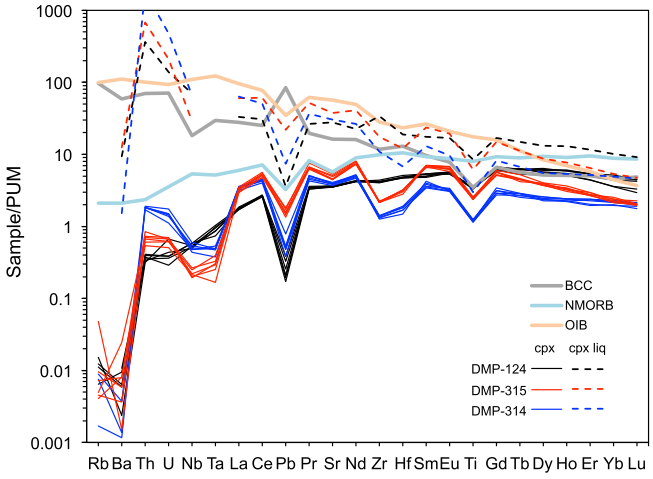

Fig. 4. Primitive-mantle normalized incompatible trace element diagram. Cpx from the studied DMP composite xenoliths are plotted as solid lines and liquids calculated to be in equilibrium with the cpx using partition coefficients from Kelemen et al. (2003) are plotted as dashed lines. Also plotted for comparison are bulk continental crust (Rudnick and Gao, 2003), N-MORB (Hofmann, 1988), and OIB (EM-1, average of Tristan lavas from GEOROC).

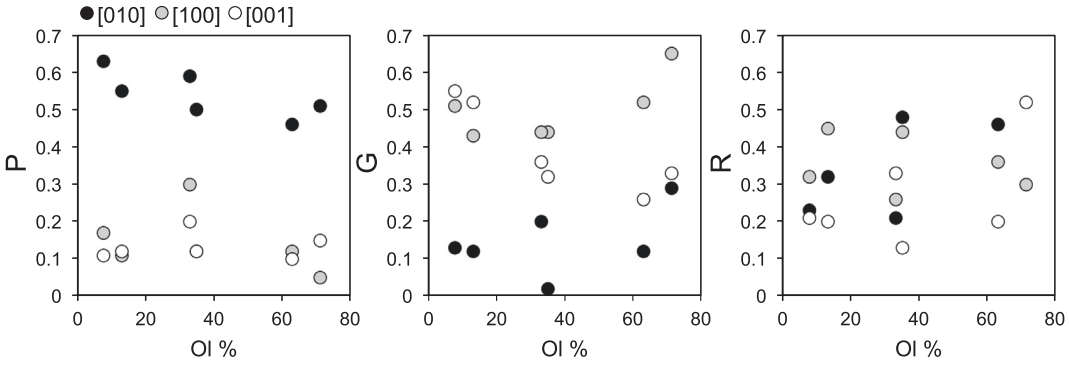

Fig. 5. Point (P), girdle (G), and random (R) components of the olivine CPO plotted as a function of olivine mode.

of CPO slightly weaker in the pyroxenitic areas (but there were also fewer olivine grains in the pyroxene-rich parts). Since olivine CPO did not vary significantly even when the map areas are separated based on lithology, we use the entire map datasets in our analysis of the results and discussion.

Two types of olivine CPO (Fig. 1c) are observed in our samples: (1) orthorhombic CPO with [0 1 0] axes perpendicular to the foliation, [1 0 0] axes clustered around the lineation and [0 0 1] axes showing a weak maximum normal to the two other axes (referred in the literature as A-type); and (2) axial-[0 1 0] or AG-type CPO where [1 0 0] and [0 0 1] axes have a girdle in the foliation and [0 1 0] is perpendicular to them. The CPO evolves with pyroxene mode. In pyroxene-poor peridotites, the CPO displays an orthorhombic pattern with a weak axial-[0 1 0] component that becomes stronger as the amount of pyroxene increases, with axial-[0 1 0] becoming dominant in olivine-poor pyroxenites (Figs. 1 and 5). An interesting aspect of the change from orthorhombic to AG-type CPOs with increasing pyroxene mode is that olivine [0 1 0] maxima become increasingly more concentrated in the pyroxene-rich xenoliths. This is quantitatively illustrated in Fig. 5 by the high values of the point component of [0 1 0] (denoted as P [0 1 0]) and concomitant low values of the point components of [1 0 0] and [0 0 1]. In addition, the girdle components of [1 0 0] and [0 0 1] (G[1 0 0] and G[0 0 1]) are elevated relative to G[0 1 0] (Fig. 5). G[0 0 1] shows a negative correlation with the olivine proportion where it increases from low values in peridotites to G[1 0 0] values in pyroxene rich samples and thus showing the evolution of the distribution from random (Fig. 5) to girdle of the [0 0 1] axes strengthening the axial-[0 1 0] pattern with increasing pyroxene mode.

4.3.2. Olivine subgrain boundaries analysis

The olivine mis2mean maps, generated using the built-in mis2mean function in MTEX, provide a measure of the intragranular misorientation: each indexed point of the crystal contains a measurement of the difference of orientation (misorientation) between the crystal average orientation and the actual measured orientation. As misorientation in crystals mostly results from the occurrence of dislocation; mis2mean maps constitute a valuable

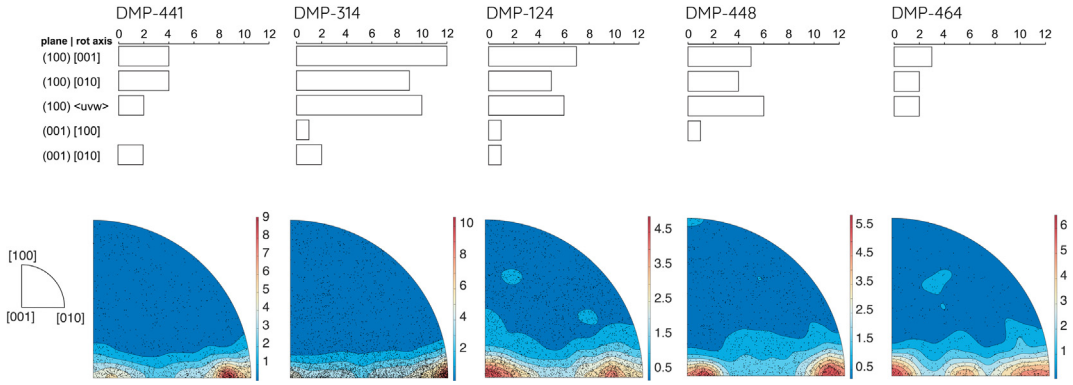

Fig. 6. Olivine intragranular misorientation data. Top row: summary of olivine subgrain boundary analysis. Bar graphs show the abundance of subgrain boundary types observed in each xenolith, the slip system may be inferred from the plane parallel to the subgrain boundary and its rotation axis, assuming the subgrain boundaries are primarily composed of edge dislocations in tilt walls. Bottom row: inverse pole figures showing distribution of rotation axis accommodating 2–10° misorientation in the olivine crystal reference frame. Individual data points omitted and contours shown for clarity.

tool to study the ductile deformation mechanisms in minerals.

Mis2mean maps (Fig. 1b) show that the amount of intragranular misorientation (and therefore degree of intracrystalline deformation) in olivine clearly decreases as pyroxene mode increases. However, the occurrence of subgrain boundaries allows us to analyze the dominant slip-system during dislocation creep (Fig. 6). The prevalence of axial-[0 1 0] olivine CPOs in the DMP composite xenoliths makes it challenging to determine which slip systems were active during plastic deformation, as the girdled distribution of [1 0 0] and [0 0 1] axes do not unambiguously point to either [1 0 0] or [0 0 1] slip. One way to better constrain the dominant slip systems during deformation is to analyze intragranular misorientation data (Fig. 1b). The analysis of subgrain boundaries orientations (see methods in Chin et al., 2016) (Fig. 6) shows that most samples have (0 1 0)[1 0 0] as dominant slip-system with {0 k l [1 0 0] and (001)[1 0 0] almost as equivalent. Slip-systems involving [0 0 1]-slip are rare. This is consistent with the inverse pole figures (IPFs) showing the distribution of rotation axes accommodating low angle misorientations in the olivine crystal reference frame (Fig. 6), which show a mix between rotation axes concentrated around [0 0 1] and [0 1 0], consistent with the subgrain analysis which shows mostly "A" and "E" type tilt boundaries.

4.3.3. Pyroxene CPO

For brevity, the pyroxene CPOs are plotted in SI Figs. 2 and 3; here we describe the general characteristics of the pyroxene CPOs as they relate to the olivine CPOs. Pyroxene CPOs, especially cpx, show more dispersed patterns compared to olivine CPOs. For the veined xenoliths (all samples except DMP-441), pyroxene [0 0 1] form weak girdles parallel to the trace of the veins and cpx [0 1 0] tends to be normal to the vein trend. Similar relationships between pyroxene CPO and vein orientations have also been observed in websterite veins cross-cutting dunite in xenoliths (Zaffarana et al., 2014; Denis et al., 2018). With the exception of DMP-441, which did not have enough pyroxene grains for a statistically significant CPO, we find that in all the xenoliths both the opx and in most cases cpx [0 0 1] is generally parallel to olivine [0 0 1] and the apparent lineation/trace of the foliation, and the opx [1 0 0], [0 1 0] or both are perpendicular to the foliation. When a pattern can be observed in the cpx CPO, it is most often the [0 1 0] axes that are normal to the foliation. It also should be noted that any pattern variation do not follow changes in composition as the olivine CPO patterns do. These pyroxene CPO patterns are commonly observed in natural upper mantle rocks.

5. DISCUSSION

5.1. Melt-rock interaction preserved in composite xenoliths – coupled geochemical & microstructural evidence

Pyroxenitic veins are commonly thought to result from refertilization and melt-rock reaction within the lithosphere (Irving, 1980; Le Roux et al., 2007; Soustelle et al., 2009), and composite peridotite-pyroxenite xenoliths are direct evidence of this process. Based on previous data (Liu et al., 2004, 2005) and our new geochemical and microstructural results, we show that the DMP composite xenoliths (1) faithfully record a last chemical equilibrium with melt, and (2) the microstructural evolution of olivine CPO is coeval with pyroxene enrichment directly resulting from melt-rock reaction.

5.2. Geochemical evidence

Whole-rock chemistry of the composite DMP xenoliths was interpreted as the result of cumulate processes (Type I) or melt-rock reaction between peridotite and silicic melt (Type II) (Liu et al., 2005). Our new mineral chemistry data support all of the above. Cpx Mg#'s are higher than olivine Mg# (Table 2), consistent with mineral-melt equilibrium (Lissenberg and Dick, 2008; Chin, 2018). The systematic change in olivine chemistry with increasing pyroxene mode (i.e. as H_2O content increases, Mg# and NiO decrease but Ti increases; Fig. 2) are also consistent with increasing melt-rock interaction (Foley et al., 2006). Rare-earth

element thermobarometry on the three xenoliths analyzed in this study for mineral chemistries, calculated at an assumed pressure of 1 GPa (Moho depths are estimated between ~28 and 42 km for this region; Huang and Xu (2010)), range from 900 °C (DMP-314), 994 °C (DMP-315), and 1002 °C (DMP-124). In contrast, major-element thermobarometry using the Brey and Kohler formulation (Brey and Kohler, 1990) range from 816 °C (DMP-314), 774 °C (DMP-315), and 1025 °C (DMP-124). The REE temperatures are high and consistent with xenolith extraction depths at the crust-mantle boundary, based on geotherms for the Hannuoba area (Huang et al., 2010) (the xenoliths fall on the geotherm). With the exception of the Type II (melt-rock reacted) DMP-124, the other Type I (cumulates) xenoliths have REE temperatures ~ 100 °C higher than temperatures recorded by major-element thermometry. The difference in temperatures from the two thermometers suggests cooling rates must have been relatively slow, as higher valence cations (e.g., 3 + REE) tend to have slower diffusivities compared to 2 + Mg, Fe, and Ca (Chin et al., 2015; Dygert and Liang, 2015). This supports an origin for a mafic underplate that accreted onto the base of the crust in Mesozoic times and subsequently cooled to the ambient geotherm.

Our measured H_2O contents in nominally anhydrous minerals also reflect last equilibration with a basaltic melt phase. Although entrainment in the host magma can often disturb primary (i.e., deep lithospheric conditions) H_2O contents of nominally anhydrous minerals in xenoliths, three lines of evidence argue against this for the DMP xenoliths. First, inter-mineral partitioning of H_2O (Fig. 3, Table 3) between olivine and pyroxenes are remarkably similar to experimental high temperature, high pressure mineral/melt D values, yet deviate from the global mantle xenolith average. The average Rcpx/opx for mantle xenoliths is 2.6 ± 0.9, in contrast to the average experimental Dcpx/opx of 1.3 ± 0.3 (Warren and Hauri, 2014). Warren and Hauri attributed this discrepancy to potentially higher H_2O fugacity (and thus higher measured water concentration) in experimental samples relative to natural ones. In addition, temperature differences and variation in cooling rates could have a strong effect in experimental vs. natural samples (Chin et al., 2016). Rcpx/opx values (averaging cores and rims) for our three analyzed Hannuoba xenoliths range from 1.81 (DMP-314), 1.76 (DMP-124), and 1.10 (DMP-315). These values are noticeably lower than the natural xenolith average, but fall well within range of experimentally constrained values. Note that the two composite xenoliths with a greater amount of pyroxenite, DMP-124 and DMP-315, approach equilibrium Dcpx/opx values more so than the peridotitic xenolith DMP-314. Although olivine/pyroxene H_2O ratios are thought to be more susceptible to diffusive re-equilibration during xenolith eruption, we found that Rol/opx and Rol/cpx do not stray far from experimental D values. Using core compositions, Rol/opx ranges from 0.11 to 0.19 (compared to experimental value 0.11 ± 0.01; Aubaud et al. (2004)) and Rol/cpx are uniform at 0.11 (compared to experimental value of 0.08 ± 0.01; Aubaud et al. (2004)). Second, we did not observe variation in H_2O content as a function of mineral grain size; a positive correlation is predicted if eruptive water loss occurred. Third, olivine grains did not show core to rim zoning in H_2O, which has also been attributed to eruption-related water loss (Demouchy et al., 2006).

Based on the above, we suggest that melt-dominated processes were primarily responsible for the observed trends in whole-rock and mineral chemistries, the calculated final equilibration temperatures, and the inter-mineral partitioning of water which are similar to experimental mineral/melt D values. In particular, olivine and cpx clearly show last equilibration with melt, in terms of their Mg# and H_2O systematics. Additionally, a positive correlation exists between cpx mode and both cpx and olivine water content (Figs. 3a and 2a, respectively). Such a correlation supports increasing precipitation of cpx as a result of crystal fractionation (e.g., crystallization of igneous cumulates) of a basaltic melt, represented by the Type I xenoliths. Alternatively, a melt-rock reaction may also produce cpx enrichment. Experimental reaction of MORB-eclogite partial melt and fertile peridotite by Mallik and Dasgupta (2012) showed that CaO decreased in melt as melt/rock ratio increased, due to increasing $D_{Ca}^{rock/melt}$ during evolution from lherzolite to websterite.

Increasing modal cpx, either from fractional crystallization and/or melt rock reaction, should also lead to increased bulk H_2O contents because cpx largely controls the water content in metasomatized peridotites (Marshall et al., 2018) In Fig. 3a, b we plot the pyroxene mode vs. pyroxene H_2O content. We observe that for low pyroxene modes (<20%) there is a near-vertical trend of increasing H_2O content in pyroxene, exemplified by natural peridotite xenoliths. Such a high variation in H_2O content but at low pyroxene modes might suggest that because these xenoliths are dominated by olivine, which has far lower H_2O capacity compared to pyroxene, late-stage fluids or cryptic metasomatic processes, which are highly enriched in incompatible elements, have an outsized effect on H_2O contents. In contrast, the slope of H_2O vs. pyroxene mode is much shallower in pyroxenites (and our composite xenoliths), particularly for clinopyroxene (Fig. 3b). This may be due to both the higher melt/rock ratio (i.e., refertilization vs. cryptic metasomatism) and the degree of melting (compared to an extremely low-F melt, the refertilizing melt will not be as highly enriched in the most incompatible elements) of the infiltrating melt experienced by the composite xenoliths.

The next question is, are the deformation microstructures in the DMP composite xenoliths also consistent with the geochemical interpretation that they formed as products of melt-rock reaction and magmatic cumulate precipitation? We address this below.

5.3. Microstructural evidence: A SPO induced CPO associated with melt-rock interaction

The main finding from analysis of the olivine CPO data is that with increasing pyroxene mode (a proxy for increasing melt/rock ratio), the CPO evolves from orthorhombic A-type to axial-[0 1 0] or AG-type CPO (Figs. 1 and 5). If the dominant deformation mechanism in the composite

Table 3
H_2O systematics in the studied DMP composite xenoliths.

	(Opx + Cpx) mode	Bulk recon. H_2O (ppm)†	Bulk recon. H_2O/Ce**	R_{core} (H_2O) Ol/Opx	R_{core} (H_2O) Ol/Cpx	R_{core} (H_2O) Cpx/Opx	H_2O equilibrium melt (wt. %)
DMP-314	35	15.5	46 (LW), 4 (PV)	0.19	0.11	1.73	0.17
DMP-124	44	24.6	36 (LW), 16 (PV)	0.17	0.11	1.58	0.27
DMP-315	88	73.9	13 (PV)	0.11	0.11	0.98	0.82
Experimental D*				0.11	0.08	1.4	

† Bulk H_2O was reconstructed from average mineral H_2O concentrations and mineral modes from EBSD maps.
* From Aubaud et al. (2004).
** Whole-rock Ce values from Liu et al. (2005); LW = lherzolite wallrock portion of composite xenolith; PV = pyroxenite vein portion of composite xenolith. We assumed the H_2O content was uniform across vein and wallrock; this is justified by the fact that mineral separates from the combined areas yielded similar H_2O contents.

xenoliths was dislocation creep and assuming a simple shear geometry, we would expect to observe orthorhombic A-type olivine CPO or axial-[1 0 0] assuming all [1 0 0]-slip slip-systems equivalent. The observed AG-type pattern could result from a strong pure shear component in the deformation geometry. This geometry would also induce a girdle distribution of the pyroxene [0 0 1] axes in the foliation plane. Such girdle, although often poorly defined, is observed for opx and rarely for cpx (Supplementary Information). However, this hypothesis may be ruled out by the fact that dislocation creep fails to explain why the CPO strength increases within the pyroxene-rich sample where AG-type forms whereas the olivine intracrystalline deformation decreases (Fig. 1). Thus, the olivine CPO variation with modal composition in our samples likely results from variation in deformation mechanisms.

If dislocation creep was the dominant deformation mechanism the evolution in CPO should be explained by change in the dominant slip systems. Yet, subgrain analyses show that [1 0 0]-slip dominates (Fig. 6) in all the composite xenoliths and cannot account for the prevalence of AG-type CPO, which would also require an equivalent activation of [0 0 1]-slip. Furthermore, we observe a decrease in the amount of intracrystalline deformation (from mis2mean maps, Fig. 1b) while the CPO strength actually increases with increasing pyroxene mode (Fig. 1c). These observations are not consistent with dislocation-creep controlled deformation.

A more likely explanation for the observed microstructural variation is an "SPO (shape preferred orientation) - induced CPO" caused by diffusion creep or grain rotation. Diffusion creep results in strong correlation between CPO and SPO (e.g., Miyazaki et al., 2013). Here, we develop a technique to test this hypothesis by plotting the long and short axis of the grain shape ellipsoid in the crystal reference frame (Fig. 7). In Fig. 7, we find a correlation between the short axis and [0 1 0] but no correlation between the long axis and any crystal direction, indicating a crystallographic control on the shape of olivine crystals that can be simulated as a flattened ellipsoid with [0 1 0] as the short axis and [1 0 0] and [0 0 1] being equivalent. Importantly, we observe that as the amount of pyroxene increases in the sample, the olivine short axis increasingly clusters around [0 1 0]. The long axis does not show preferred orientation except for sample DMP464 where it is close to [0 0 1]. This shows that as the amount of pyroxene increases the olivine crystals saw their shortest axis parallel to [0 1 0] aligned normal to the foliation without preferred orientation for [1 0 0] and [0 0 1] inducing the AG-type CPO and therefore demonstrating that it is a SPO-induced CPO.

Several previous studies have shown deformation of olivine in presence of significant amounts of melt results in the development of AG-type CPO (Holtzman et al., 2003; Higgie and Tommasi, 2012; Chin et al., 2016). Recently, Qi et al. (2018) investigated the effect of melt on olivine CPO development and observed the development of AG-type CPO with strong point component for [1 0 0] and [0 0 1] with the latter aligning with the shear direction. They suggested a combination of mechanisms to explain their CPO composed of (1) a crystallographically controlled

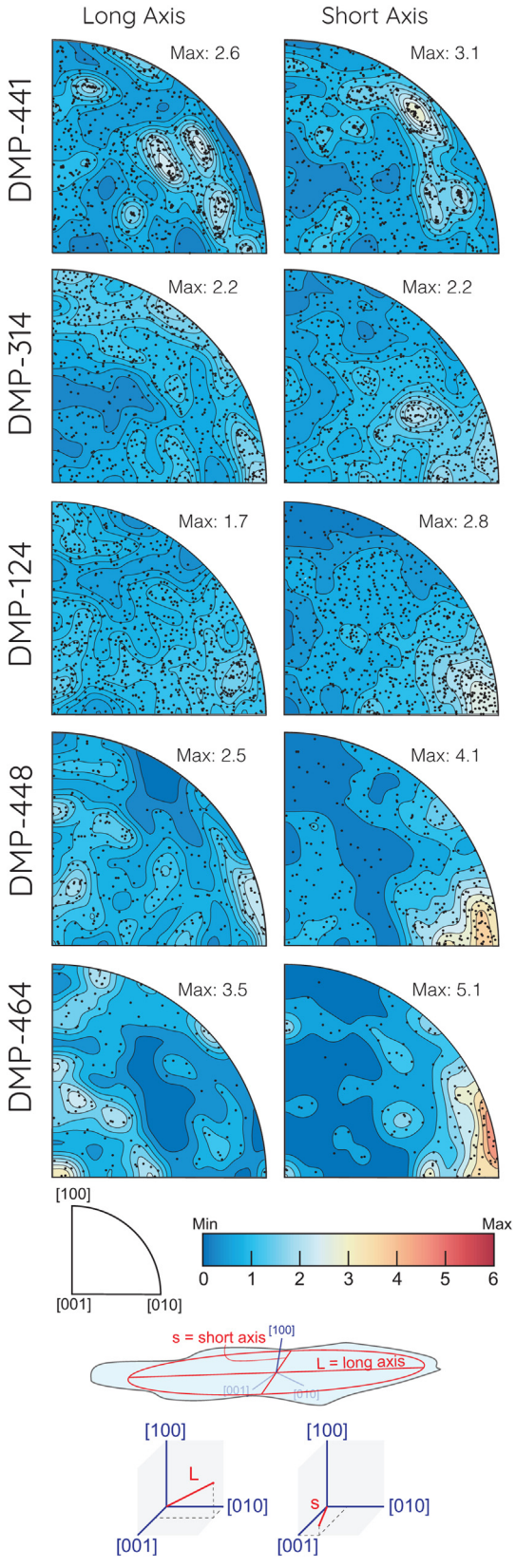

Fig. 7. Inverse pole figures in the olivine crystal reference frame of the long and short axes of the shape ellipsoid calculated for all olivine grains in every sample (lower hemisphere, equal-area projection, contours at one multiple of uniform distribution).

SPO-induced CPO leading to [0 1 0] normal to the shear plane and [0 0 1] parallel to the shear-direction; and (2) dislocation glide on the (0 1 0)[1 0 0] slip-system leading to a clustering of [1 0 0] axes parallel to the shear direction with [0 0 1] axes in the shear plane normal to shear direction. This competition results in a weak concentration of shear-normal [1 0 0] axes. Our observations are mostly consistent with Qi et al. (2018), however the contribution of dislocation creep to the CPO development in olivine-poor pyroxenite is likely very weak as P[1 0 0] and P[0 0 1] are very low (Fig. 5).

With increasing melt-rock interaction and crystallization of the melt as new secondary phases such as pyroxene, the olivine deformation mechanism may evolve from dislocation creep to diffusion creep (Sundberg and Cooper, 2008; Soustelle and Manthilake, 2017) and affect the development of its CPO. However, diffusion creep (in monomineralic aggregates) leads to a strong correlation between CPO and SPO (e.g., Miyazaki et al., 2013) and could also be consistent with our observations, without the need for deformation occurring in the presence of melt. Occurrence of diffusion creep (in the absence of melt) in the DMP composite xenoliths is questionable, though, owing to the relatively large grain size and the occurrence of numerous intracrystalline microstructures (Fig. 1b). Furthermore, the geochemical and textural characteristics of the composite xenoliths clearly show they formed by infiltration of melt into peridotite (Type II) or as magmatic cumulates (Type I).

5.4. A unified hypothesis integrating both geochemical & microstructural datasets

Our preferred hypothesis, which reconciles both geochemical and microstructural data, invokes a necessary role for presence of melt and melt-rock reaction to induce the observed SPO-induced CPO (e.g. Qi et al., 2018). We show a cartoon of the process envisioned in Fig. 8, which is generally applicable to composite xenoliths (cf. Irving, 1980) formed through sustained melt-rock interaction. Melt infiltrating through peridotitic lithosphere (green region) is focused in a porous flow channel (yellow region), resulting in reaction of the melt with olivine and crystallization of pyroxene. As a result of the reaction, olivine grain size is reduced as new pyroxene is formed. At high melt/rock ratios, olivine grains rotate with their flattest (0 1 0) faces aligned with magmatic flow. We note that Wheeler et al. (2001) suggested a similar scenario for olivine in layered mafic intrusions, where olivine grains gravitationally settle on the relatively large and flat (0 1 0) faces, resulting in a CPO with a girdled distribution of [1 0 0] but strong point maxima of [0 1 0] normal to foliation. Wen et al. (2018) also noted a similar olivine SPO-induced CPO in olivine crystals crystallizing from mafic melt (e.g. in a magma). The most pyroxene-rich xenoliths (and thus those with highest melt/rock ratio, e.g. DMP-315) show the strongest concentration of [0 1 0] maxima normal to the trace of the (magmatic) foliation (Fig. 1c), and the strongest concentration of [0 1 0] aligned with the short axis in olivine (Figs. 7,8). By contrast, the xenoliths with less pyroxene (and thus lower melt/rock ratios) show weaker [0 1 0] maxima normal to

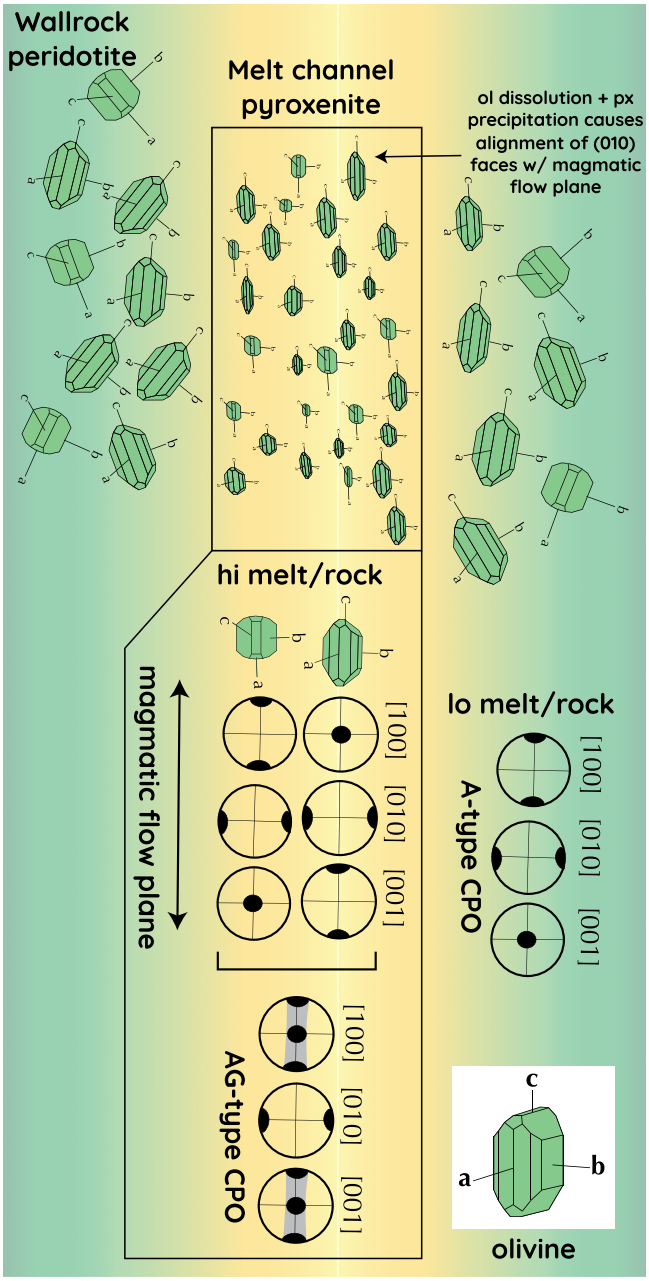

Fig. 8. Cartoon illustrating our proposed mechanism for generating an SPO-induced CPO as a result of melt-rock reaction (see text for full explanation).

the trace of the foliation (Fig. 1c) and no preferred orientation of the long axis in olivine (Fig. 7). Finally, although the correlation is relatively weak, olivines with higher aspect ratio tend to cluster closer to the trace of the foliation/veins (SI Fig. 4), supporting rotation of grains in the melt-induced foliation.

5.5. Nature and origin of the infiltrating melts

Lastly, we speculate on the nature and origin of the melt (s) that infiltrated the host peridotites of the DMP xenolith suite to generate the observed composite peridotite/pyroxenite xenoliths. Modal cpx increases as olivine H_2O increases and olivine Mg# decreases (Fig. 3a), consistent with increasing melt/rock ratio (Ionov et al., 2005). Melts calculated to be in equilibrium with cpx (using partition coefficients from Kelemen et al. (2003)) in the DMP xenoliths show highly fractionated trace element patterns intermediate between bulk continental crust (BCC, Rudnick and Gao, 2003) and EM-1 oceanic island basalts (OIB; here we plotted the average of all Tristan de Cunha lavas, type locale for EM-1, from GEOROC online database). Cpx-melts are clearly distinct from melts of depleted mantle (N-MORB; Hofmann, 1988) (Fig. 4). Liu et al. (2005) pro-

posed that the infiltrating melts for the DMP composite xenoliths were silicic and potentially derived from either melting of foundered mafic lower crust or melting of fossil oceanic slabs accreted beneath the NCC. This interpretation fits with the calculated cpx-melt trace element patterns, indicating a crustal origin for the melts that infiltrated the NCC mantle lithosphere. An origin of the infiltrating melt from an EM-1 type source is also possible, as isotopic compositions of some peridotite xenoliths from Hannuoba plot towards EM-1 in terms of Sr and Nd isotopes (Xu et al., 2008). Moreover, EM-type mantle heterogeneities are thought to share a common origin from recycled continental crust (Willbold and Stracke, 2010). However, further isotopic data are needed on the DMP composite xenoliths to draw a more robust connection to an EM-1 source. Nonetheless, a crustal origin for the infiltrating melt appears robust.

We now discuss the hydration state of the infiltrating melt. For such highly melt-rock reacted xenoliths, the water contents in pyroxenes and bulk rocks, reconstructed using mineral modes from EBSD maps and average mineral compositions (Table 3) plot at the low end compared to other peridotites and pyroxenites from the literature (Fig. 3). We note that there are few systematic studies of pyroxenite xenolith H_2O contents in the literature compared to peridotite xenolith H_2O studies (the peridotite data plotted in Fig. 3). Pyroxenite suites from several localities in the NCC show wide ranges of bulk rock H_2O contents, ranging from ~20 to 300 ppm for Cr-pyroxenites, ~40 to 100 ppm for Al-pyroxenites, and ~40 to 70 ppm for garnet pyroxenites (Hao et al., 2018). The range for reconstructed bulk rock DMP composite xenoliths in this study is 16 – 74 ppm (Table 3). By contrast, pyroxenites from Hawaii have high bulk H_2O contents, ~300 ppm on average (Bizimis and Peslier, 2015). We note that the Hawaii pyroxenites were reported to contain small amounts of phlogopite, whereas the DMP xenoliths, both those reported in Hao et al. (2018) and this study, do not contain phlogopite.

High H_2O contents tend to be correlated with increased metasomatism and melt-rock reaction in the mantle (Peslier et al., 2012; Doucet et al., 2014), so the low H_2O observed in DMP pyroxenites but the inferred high melt/rock ratios appear paradoxical. H_2O contents of melts calculated to be in equilibrium with bulk DMP xenoliths, using partition coefficients from (Aubaud et al., 2004) have <1 wt.% H_2O. Such low melt H_2O implies that the source of the melts was not particularly hydrous. For example, assuming a bulk peridotite DH_2O of 0.009 (Aubaud et al., 2004), 1% partial melting of the most hydrous mantle reservoir (FOZO with 750 ppm H_2O; Dixon et al., 2002) would yield a melt with 4 wt.% H_2O (note that, because H_2O is highly incompatible, its effect on partial melting is most pronounced at low melt fractions; e.g. Asimow and Langmuir, 2003). A 1% melt of primitive mantle (330 ppm; Dixon and Clague, 2001) would result in a melt with 1.75 wt.% H_2O, and a 1% melt of depleted MORB mantle (assuming 70 ppm (Dixon and Clague, 2001)) would yield a melt with 0.4 wt.% H_2O. While the H_2O content of a DMM-derived melt overlaps that calculated for the DMP xenoliths (0.17–0.82 wt.% H_2O), the melts calculated to be in equilibrium with cpx (Fig. 4) are not consistent with derivation from a DMM source.

Yang et al. (2008) reported bulk H_2O of granulite xenoliths from Hannuoba, NCC ranging from 160 to 360 ppm H_2O. Using the lower end of this range, a 1% melt of the Hannuoba granulite source results in a melt with 0.85 wt.% H_2O, similar to the most hydrous melt (0.82 wt.%) calculated to be in equilibrium with cpx in the DMP composite xenoliths (Table 3). This supports the hypothesis that foundered lower crust or dehydrated, eclogitized oceanic crust could be potential melt sources in the DMP composite xenoliths (Liu et al., 2005), as both of these crustal sources could be simultaneously trace-element enriched but water-poor because of high-grade metamorphism and previous melt depletion. Note, also that the EM-1 source is estimated to have 160–220 ppm H_2O (Bizimis and Peslier, 2015); these values overlap the H_2O range of Hannuoba granulites discussed above.

Recently, Chen et al. (2017) suggested that the last metasomatic event beneath the vicinity of the Hannuoba basalts involved infiltration of CO_2-rich silicate melts linked to melting of subducted carbonate sediments in the Cenozoic. Experiments on solubility of H_2O-CO_2 fluids at mantle conditions indicates that a mixed H_2O-CO_2 fluid phase can lower the solubility of H_2O in olivine by as much as a factor of 4 (Yang et al., 2014). Thus, one potential explanation for the paradoxical nature of the DMP melt infiltration could be the presence of some CO_2 in the melt. This could explain why the most pyroxene-rich composite xenoliths appear to have formed at high melt/rock ratios by an "enriched" melt (in terms of incompatible trace elements) that was simultaneously very dry. Finally, we note that the H_2O/Ce ratios of DMP composite xenoliths are low (4–46; Table 3) compared to Hawaii (59–92) but similar to other Hannuoba pyroxenites (0.4–42; Hao et al., 2018). Bizimis and Peslier (2015) showed that DCe cpx is higher than DH_2O cpx despite canonical knowledge that DCe ~ DH_2O in the bulk upper mantle (Michael, 1995). The low H_2O/Ce in DMP composite xenoliths is therefore consistent with infiltration by a melt that had higher trace element (i.e. Ce) contents but low H_2O.

6. SUMMARY & IMPLICATIONS

We summarize the two key findings of our integrated geochemical and microstructural investigation of composite mantle xenoliths below:

- Composite peridotite/pyroxenite xenoliths from Damaping, Hannuoba, NCC record low water contents in pyroxene and olivine, despite evidence that these xenoliths were significantly melt-rock reacted and/or products of magmatic cumulating processes. To reconcile this apparent paradox, we propose that the infiltrating melt was simultaneously trace-element enriched but dry. Possible origins for the infiltrating melt include foundered lower crust beneath the NCC or an EM-1 type mantle source, or, a CO_2-rich silicate melt from recent subduction. All of these sources would have rela-

tively low H_2O contents while being potentially rich in trace elements (e.g., having a continental crust signature). Our study adds to growing evidence that water and metasomatism are often decoupled.

- Collectively, the systematic variation in CPO strength, particularly the coeval increase in [0 1 0] maxima with increasing pyroxene mode and the progressively girdled distribution of [1 0 0] and [0 0 1] in the foliation plane is consistent with a model wherein olivine grains rotate to have their flattest faces aligning with the melt flow direction. Grain rotation thus occurs via diffusion creep at grain boundaries or grain-boundary sliding; both of these processes are facilitated by increasing melt/rock ratios. These results are the first, to our knowledge, clear natural evidence for SPO-induced CPO in deep lithospheric xenoliths.

Our study has implications for the interpretation of composite mantle xenoliths, which are widely thought to be direct evidence of melt-rock interaction in the mantle lithosphere. We show that increasing extent of melt infiltration causes a systematic change in olivine CPO, leading to an SPO-induced CPO that previously was only recognized in shallow intrusions and mafic melts. More importantly, the recognition of an SPO-induced CPO resulting from melt infiltration indicates that measurable olivine CPO can be generated in the absence of dislocation creep.

ACKNOWLEDGMENTS

We thank Joseph Boesenberg and Soumen Mallick for assistance on the electron microprobe and laser ablation ICP-MS, respectively. We also thank Yunbin Guan for assistance on the SIMS. We express gratitude to Andrea Tommasi and two anonymous reviewers for their constructive comments that helped improve the manuscript, Guest Associate Editor Sonja Aulbach, Associate Editor Fang-Zhen Teng, and Execute Editor Jeffrey Catalano for their patience and efficiency in handling our manuscript. EJC acknowledges funding from NSF EAR 1719208.

APPENDIX A. SUPPLEMENTARY MATERIAL

Supplementary data to this article can be found online at https://doi.org/10.1016/j.gca.2019.10.002.

REFERENCES

Asimow P. D. and Langmuir C. H. (2003) The importance of water to oceanic mantle melting regimes. *Nature* **421**, 815.

Aubaud C., Hauri E. H. and Hirschmann M. M. (2004) Hydrogen partition coefficients between nominally anhydrous minerals and basaltic melts. *Geophys. Res. Lett.* **31**.

Aubaud C., Withers A. C., Hirschmann M. M., Guan Y., Leshin L. A., Mackwell S. J. and Bell D. R. (2007) Intercalibration of FTIR and SIMS for hydrogen measurements in glasses and nominally anhydrous minerals. *Am. Mineral.* **92**, 811–828.

Bachmann F., Hielscher R. and Schaeben H. (2011) Grain detection from 2d and 3d EBSD data: specification of the MTEX algorithm. *Ultramicroscopy* **111**, 1720–1733.

Baptiste V. and Tommasi A. (2014) Petrophysical constraints on the seismic properties of the Kaapvaal craton mantle root. *Solid Earth* **5**, 45–63.

Bascou J., Doucet L. S., Saumet S., Ionov D. A., Ashchepkov I. V. and Golovin A. V. (2011) Seismic velocities, anisotropy and deformation in Siberian cratonic mantle: EBSD data on xenoliths from the Udachnaya kimberlite. *Earth Planet. Sci. Lett.* **304**, 71–84.

Ben Ismail W. and Mainprice D. (1998) An olivine fabric database: an overview of upper mantle fabrics and seismic anisotropy. *Tectonophysics* **296**, 145–157.

Bernard R. E., Behr W. M., Becker T. W. and Young D. J. (2019) Relationships between olivine CPO and deformation parameters in naturally deformed rocks and implications for mantle seismic anisotropy. *Geochemistry Geophysics Geosystems* **20**, 3469–3494. https://doi.org/10.1029/2019GC008289.

Best M. (1975) Amphibole-bearing cumulate inclusions, Grand Canyon, Arizona and their bearing on silica-undersaturated hydrous magmas in the upper mantle. *J. Petrol.* **16**, 212–236.

Bizimis M. and Peslier A. H. (2015) Water in Hawaiian garnet pyroxenites: implications for water heterogeneity in the mantle. *Chem. Geol.* **397**, 61–75.

Bodinier J.-L. and Godard M. (2003) Orogenic, ophiolitic, and abyssal peridotites. *Treatise Geochem.* **2**, 568.

Brey G. P. and Kohler T. (1990) Geothermobarometry in four-phase lherzolites II. New thermobarometers, and practical assessment of existing thermobarometers. *J. Petrol.* **31**, 1353–1378.

Bunge H. (1982) *Texture Analysis in Materials Science*. Butterworth's, London.

Chen C., Liu Y., Foley S. F., Ducea M. N., Geng X., Zhang W., Xu R., Hu Z., Zhou L. and Wang Z. (2017) Carbonated sediment recycling and its contribution to lithospheric refertilization under the northern North China Craton. *Chem. Geol.* **466**, 641–653.

Chen C. and Presnall D. (1975) The system Mg2SiO4-SiO2 at pressures up to 25 kilobars. *Am. Mineral.* **60**, 398–406.

Chin E. J. (2018) Deep crustal cumulates reflect patterns of continental rift volcanism beneath Tanzania. *Contrib. Miner. Petrol.* **173**, 85.

Chin E. J., Lee C. T. A. and Blichert-Toft J. (2015) Growth of upper plate lithosphere controls tempo of arc magmatism: Constraints from Al-diffusion kinetics and coupled Lu-Hf and Sm-Nd chronology. *Geochem. Perspect. Lett.* **1**, 20–32.

Chin E. J., Soustelle V., Hirth G., Saal A. E., Kruckenberg S. C. and Eiler J. M. (2016) Microstructural and geochemical constraints on the evolution of deep arc lithosphere. *Geochem. Geophys. Geosyst.* **17**, 2497–2521. https://doi.org/10.1002/2015GC006156.

Dawson J. (1984) *Contrasting Types of Upper-Mantle Metasomatism? Developments in Petrology*. Elsevier, pp. 289–294.

Demouchy S. and Bolfan-Casanova N. (2016) Distribution and transport of hydrogen in the lithospheric mantle: a review. *Lithos* **240**, 402–425.

Demouchy S., Jacobsen S. D., Gaillard F. and Stern C. R. (2006) Rapid magma ascent recorded by water diffusion profiles in mantle olivine. *Geology* **34**, 429–432.

Denis C. M., Demouchy S. and Alard O. (2018) Heterogeneous hydrogen distribution in orthopyroxene from veined mantle peridotite (San Carlos, Arizona): impact of melt-rock interactions. *Lithos* **302**, 298–311.

Dijkstra A. H., Drury M. R., Vissers R. L. and Newman J. (2002) On the role of melt-rock reaction in mantle shear zone formation in the Othris Peridotite Massif (Greece). *J. Struct. Geol.* **24**, 1431–1450.

Dixon J. E. and Clague D. A. (2001) Volatiles in basaltic glasses from Loihi Seamount, Hawaii: evidence for a relatively dry plume component. *J. Petrol.* **42**, 627–654.

Dixon J. E., Leist L., Langmuir C. and Schilling J.-G. (2002) Recycled dehydrated lithosphere observed in plume-influenced mid-ocean-ridge basalt. *Nature* **420**, 385.

Doucet L. S., Peslier A. H., Ionov D. A., Brandon A. D., Golovin A. V., Goncharov A. G. and Ashchepkov I. V. (2014) High water contents in the Siberian cratonic mantle linked to metasomatism: an FTIR study of Udachnaya peridotite xenoliths. *Geochim. Cosmochim. Acta* **137**, 159–187.

Dygert N. and Liang Y. (2015) Temperatures and cooling rates recorded in REE in coexisting pyroxenes in ophiolitic and abyssal peridotites. *Earth Planet. Sci. Lett.* **420**, 151–161.

Fernández-Roig M., Galán G. and Mariani E. (2017) Deformation and seismic anisotropy of the subcontinental lithospheric mantle in NE Spain: EBSD data on xenoliths from the Catalan Volcanic Zone. *Tectonophysics* **698**, 16–37.

Foley S., Andronikov A., Jacob D. and Melzer S. (2006) Evidence from Antarctic mantle peridotite xenoliths for changes in mineralogy, geochemistry and geothermal gradients beneath a developing rift. *Geochim. Cosmochim. Acta* **70**, 3096–3120.

Foley S. F. (2008) Rejuvenation and erosion of the cratonic lithosphere. *Nat. Geosci.* **1**, 503.

Gao S., Rudnick R. L., Carlson R. W., McDonough W. F. and Liu Y.-S. (2002) Re–Os evidence for replacement of ancient mantle lithosphere beneath the North China craton. *Earth Planet. Sci. Lett.* **198**, 307–322.

Griffin W. L., Andi Z., O'reilly S. and Ryan C. (1998) Phanerozoic evolution of the lithosphere beneath the Sino-Korean craton. *Mantle Dyn. Plate Interact. East Asia* **27**, 107–126.

Hao Y.-T., Li P., Coltorti M. and Xia Q.-K. (2018) Variations in the H2O content and H2O/Ce ratio of mantle pyroxenites: implications for enriched components in the mantle. *J. Geophys. Res. Solid Earth* **123**, 5628–5643.

Harte B. (1983) Mantle peridotites and processes the kimberlites sample. *Continental Basalts Mantle Xenoliths*, 46–91.

Harte B., Gurney J. and Cox K. (1977) Clinopyroxene-rich sheets in garnet-peridotite: xenolith specimens from the Matsoku kimberlite pipe. In Lesotho, International Kimberlite Conference: Extended Abstracts, pp. 138–140.

Hidas K., Falus G., Szabó C., Szabó P. J., Kovács I. and Földes T. (2007) Geodynamic implications of flattened tabular equigranular textured peridotites from the Bakony-Balaton Highland Volcanic Field (Western Hungary). *J. Geodyn.* **43**, 484–503.

Hielscher R. and Schaeben H. (2008) A novel pole figure inversion method: specification of the MTEX algorithm. *J. Appl. Crystallogr.* **41**, 1024–1037.

Higgie K. and Tommasi A. (2012) Feedbacks between deformation and melt distribution in the crust-mantle transition zone of the Oman ophiolite. *Earth Planet. Sci. Lett.* **359**, 61–72.

Higgie K. and Tommasi A. A. (2014) Deformation in a partially molten mantle: constraints from plagioclase lherzolites from Lanzo, western Alps. *Tectonophysics* **615**, 167–181.

Hofmann A. W. (1988) Chemical differentiation of the Earth: the relationship between mantle, continental crust, and oceanic crust. *Earth Planet. Sci. Lett.* **90**, 297–314.

Holtzman B., Kohlstedt D., Zimmerman M., Heidelbach F., Hiraga T. and Hustoft J. (2003) Melt segregation and strain partitioning: implications for seismic anisotropy and mantle flow. *Science* **301**, 1227–1230.

Huang X. and Xu Y. (2010) Thermal state and structure of the lithosphere beneath eastern China: a synthesis on basalt-borne xenoliths. *J. Earth Sci.* **21**, 711–730.

Hui H., Peslier A. H., Rudnick R. L., Simonetti A. and Neal C. R. (2015) Plume-cratonic lithosphere interaction recorded by water and other trace elements in peridotite xenoliths from the Labait volcano. *Tanzania. Geochem., Geophys., Geosyst.* **16**, 1687–1710.

Ionov D., Chanefo I. and Bodinier J.-L. (2005) Origin of Fe-rich lherzolites and wehrlites from Tok, SE Siberia by reactive melt percolation in refractory mantle peridotites. *Contrib. Miner. Petrol.* **150**, 335–353.

Irving A. (1974) Geochemical and high pressure experimental studies of garnet pyroxenite and pyroxene granulite xenoliths from the Delegate basaltic pipes, Australia. *J. Petrol.* **15**, 1–40.

Irving A. J. (1980) Petrology and geochemistry of composite ultramafic xenoliths in alkalic basalts and implications for magmatic processes within the mantle. *Am. J. Sci.* **280**, 389–426.

Jordan T. H. (1979) Mineralogies, densities and seismic velocities of garnet lherzolites and their geophysical implications. *Mantle Sample: Inclusion Kimberlites Volcan.* **16**, 1–14.

Jung S., Jung H. and Austrheim H. (2014) Characterization of olivine fabrics and mylonite in the presence of fluid and implications for seismic anisotropy and shear localization. *Earth Planets Space* **66**, 46.

Kelemen P. B. (1990) Reaction between ultramafic rock and fractionating basaltic magma I. Phase relations, the origin of calc-alkaline magma series, and the formation of discordant dunite. *J. Petrol.* **31**, 51–98.

Kelemen P. B., Dick H. J. and Quick J. E. (1992) Formation of harzburgite by pervasive melt/rock reaction in the upper mantle. *Nature* **358**, 635.

Kelemen P. B., Yogodzinski G. M. and Scholl D. W. (2003) Along-strike variation in the Aleutian island arc: genesis of high Mg# andesite and implications for continental crust. Inside the Subduction Factory. *Geophys. Monogr. Ser* **138**, 223–276.

Kusky T., Polat A., Windley B. F., Burke K., Dewey J., Kidd W., Maruyama S., Wang J., Deng H. and Wang Z. (2016) Insights into the tectonic evolution of the North China Craton through comparative tectonic analysis: a record of outward growth of Precambrian continents. *Earth Sci. Rev.* **162**, 387–432.

Le Roux V., Bodinier J. L., Tommasi A., Alard O., Dautria J. M., Vauchez A. and Riches A. J. V. (2007) The Lherz spinel lherzolite: refertilized rather than pristine mantle. *Earth Planet. Sci. Lett.* **259**, 599–612.

Lissenberg C. J. and Dick H. J. (2008) Melt–rock reaction in the lower oceanic crust and its implications for the genesis of mid-ocean ridge basalt. *Earth Planet. Sci. Lett.* **271**, 311–325.

Liu D., Nutman A., Compston W., Wu J. and Shen Q. H. (1992) Remnants of≥ 3800 Ma crust in the Chinese part of the Sino-Korean craton. *Geology* **20**, 339–342.

Liu Y., Gao S., Hu Z., Gao C., Zong K. and Wang D. (2010) Continental and oceanic crust recycling-induced melt–peridotite interactions in the Trans-North China Orogen: U-Pb dating, Hf isotopes and trace elements in zircons from mantle xenoliths. *J. Petrol.* **51**, 537–571.

Liu Y., Gao S., Lee C.-T. A., Hu S., Liu X. and Yuan H. (2005) Melt–peridotite interactions: links between garnet pyroxenite and high-Mg# signature of continental crust. *Earth Planet. Sci. Lett.* **234**, 39–57.

Liu Y., Gao S., Liu X., Chen X., Zhang W. and Wang X. (2003) Thermodynamic evolution of lithosphere of the North China craton: records from lower crust and upper mantle xenoliths from Hannuoba. *Chin. Sci. Bull.* **48**, 2371–2377.

Liu Y., Gao S., Yuan H., Zhou L., Liu X., Wang X., Hu Z. and Wang L. (2004) U-Pb zircon ages and Nd, Sr, and Pb isotopes of lower crustal xenoliths from North China Craton: insights on evolution of lower continental crust. *Chem. Geol.* **211**, 87–109.

Liu Y., He D., Gao C., Foley S., Gao S., Hu Z., Zong K. and Chen H. (2015) First direct evidence of sedimentary carbonate recycling in subduction-related xenoliths. *Sci. Rep.* **5**, 11547.

Li P., Xia Q.-K., Deloule E., Chen H., Gu X.-Y. and Feng M. (2015) Temporal variation of H_2O content in the lithospheric

mantle beneath the eastern North China Craton: Implications for the destruction of cratons. *Gondwana Research* **28**, 276–287.
Mainprice D., Bachmann F., Hielscher R. and Schaeben H. (2015) Descriptive tools for the analysis of texture projects with large datasets using MTEX: strength, symmetry and components. *Geol. Soc., London, Special Publ.* **409**, 251–271.
Mainprice D., Tommasi A. A., Couvy H. I., Cordier P. and Frost D. J. (2005) Pressure sensitivity of olivine slip systems and seismic anisotropy of Earth's upper mantle. *Nature* **433**, 731–733.
Mallik A. and Dasgupta R. (2012) Reaction between MORB-eclogite derived melts and fertile peridotite and generation of ocean island basalts. *Earth Planet. Sci. Lett.* **329**, 97–108.
Marshall E. W., Lassiter J. C. and Barnes J. D. (2018) On the (mis) behavior of water in the mantle: controls on nominally anhydrous mineral water content in mantle peridotites. *Earth Planet. Sci. Lett.* **499**, 219–229.
Menzies M. A., Fan W. and Zhang M. (1993) Palaeozoic and Cenozoic lithoprobes and the loss of >120 km of Archaean lithosphere, Sino-Korean craton, China. *Geol. Soc., London, Special Publ.* **76**, 71–81.
Michael P. (1995) Regionally distinctive sources of depleted MORB: Evidence from trace elements and H2O. *Earth Planet. Sci. Lett.* **131**, 301–320.
Miyazaki T., Sueyoshi K. and Hiraga T. (2013) Olivine crystals align during diffusion creep of Earth/'s upper mantle. *Nature* **502**, 321–326.
Morse S. A. (1980) *Basalts and Phase Diagrams: An Introduction to the Quantitative Use of Phase Diagrams in Igneous Petrology*. Springer Verlag.
Mosenfelder J. L., Le Voyer M., Rossman G. R., Guan Y., Bell D. R., Asimow P. D. and Eiler J. M. (2011) Analysis of hydrogen in olivine by SIMS: evaluation of standards and protocol. *Am. Mineral.* **96**, 1725–1741.
Mosenfelder J. L. and Rossman G. R. (2013a) Analysis of hydrogen and fluorine in pyroxenes: I. Orthopyroxene. *Am. Mineral.* **98**, 1026–1041.
Mosenfelder J. L. and Rossman G. R. (2013b) Analysis of hydrogen and fluorine in pyroxenes: II. Clinopyroxene. *Am. Mineral.* **98**, 1042–1054.
Naif S., Key K., Constable S. and Evans R. (2013) Melt-rich channel observed at the lithosphere–asthenosphere boundary. *Nature* **495**, 356.
Nielson J. E. and Noller J. S. (1987) Processes of mantle metasomatism; constraints from observations of composite peridotite xenoliths. Mantle metasomatism and alkaline magmatism. Geol. Society of America, Inc. Publ, pp. 61–76.
O'Reilly S. Y. and Griffin W. (2013) *Mantle Metasomatism. Metasomatism and the Chemical Transformation of Rock*. Springer, pp. 471–533.
Pearson D., Canil D. and Shirey S. (2003) Mantle samples included in volcanic rocks: xenoliths and diamonds. *Treatise Geochem.* **2**, 171–275.
Peslier A. H., Schönbächler M., Busemann H. and Karato S.-I. (2017) Water in the earth's interior: distribution and origin. *Space Sci. Rev.* **212**, 743–810.
Peslier A. H., Woodland A. B., Bell D. R., Lazarov M. and Lapen T. J. (2012) Metasomatic control of water contents in the Kaapvaal cratonic mantle. *Geochim. Cosmochim. Acta* **97**, 213–246.
Qi C., Hansen L. N., Wallis D., Holtzman B. K. and Kohlstedt D. L. (2018) Crystallographic preferred orientation of olivine in sheared partially molten rocks: the source of the "a-c switch". *Geochem. Geophys. Geosyst.* **19**, 316–336.
Rampone E., Piccardo G. B. and Hofmann A. W. (2008) Multi-stage melt–rock interaction in the Mt. Maggiore (Corsica, France) ophiolitic peridotites: microstructural and geochemical evidence. *Contrib. Miner. Petrol.* **156**, 453–475.
Rudnick R. L. and Gao S. (2003) Composition of the continental crust. *Treatise Geochem.* **3**, 1–64.
Rudnick R. L., Gao S., Ling W.-L., Liu Y.-S. and McDonough W. F. (2004) Petrology and geochemistry of spinel peridotite xenoliths from Hannuoba and Qixia, North China craton. *Lithos* **77**, 609–637.
Schmerr N. (2012) The Gutenberg discontinuity: melt at the lithosphere-asthenosphere boundary. *Science* **335**, 1480–1483.
Schutt D. L. and Lesher C. E. (2010) Compositional trends among Kaapvaal Craton garnet peridotite xenoliths and their effects on seismic velocity and density. *Earth Planet. Sci. Lett.* **300**, 367–373.
Sen G. (1988) Petrogenesis of spinel lherzolite and pyroxenite suite xenoliths from the Koolau shield, Oahu, Hawaii: implications for petrology of the post-eruptive lithosphere beneath Oahu. *Contrib. Miner. Petrol.* **100**, 61–91.
Simon N. S., Irvine G. J., Davies G. R., Pearson D. G. and Carlson R. W. (2003) The origin of garnet and clinopyroxene in "depleted" Kaapvaal peridotites. *Lithos* **71**, 289–322.
Soustelle V. and Manthilake G. (2017) Deformation of olivine-orthopyroxene aggregates at high pressure and temperature: implications for the seismic properties of the asthenosphere. *Tectonophysics* **694**, 385–399.
Soustelle V. and Tommasi A. (2010) Seismic properties of the supra-subduction mantle: constraints from peridotite xenoliths from the Avacha volcano, southern Kamchatka. *Geophys. Res. Lett.* **37**.
Soustelle V., Tommasi A., Bodinier J.-L., Garrido C. and Vauchez A. (2009) Deformation and reactive melt transport in the mantle lithosphere above a large-scale partial melting domain: the Ronda Peridotite Massif, Southern Spain. *J. Petrol.* **50**, 1235–1266.
Soustelle V., Tommasi A., Demouchy S. and Ionov D. (2010) Deformation and fluid-rock interaction in the supra-subduction mantle: microstructures and water contents in peridotite xenoliths from the Avacha Volcano, Kamchatka. *J. Petrol.* **51**, 363–394.
Sundberg M. and Cooper R. F. (2008) Crystallographic preferred orientation produced by diffusional creep of harzburgite: effects of chemical interactions among phases during plastic flow. *J. Geophys. Res.: Solid Earth (1978, Âì2012)* **113**.
Tang Y.-J., Zhang H.-F., Ying J.-F. and Su B.-X. (2013) Widespread refertilization of cratonic and circum-cratonic lithospheric mantle. *Earth Sci. Rev.* **118**, 45–68.
Tharimena S., Rychert C. and Harmon N. (2017) A unified continental thickness from seismology and diamonds suggests a melt-defined plate. *Science* **357**, 580–583.
Tommasi A., Mainprice D., Canova G. and Chastel Y. (2000) Viscoplastic self-consistent and equilibrium-based modeling of olivine lattice preferred orientations: implications for the upper mantle seismic anisotropy. *J. Geophys. Res.: Solid Earth (1978–2012)* **105**, 7893–7908.
Tommasi A. A., Tikoff B. and Vauchez A. (1999) Upper mantle tectonics: three-dimensional deformation, olivine crystallographic fabrics and seismic properties. *Earth Planet. Sci. Lett.* **168**, 173–186.
Tommasi A. A., Vauchez A. and Ionov D. A. (2008) Deformation, static recrystallization, and reactive melt transport in shallow subcontinental mantle xenoliths (Tok Cenozoic volcanic field, SE Siberia). *Earth Planet. Sci. Lett.* **272**, 65–77.
Tursack E. and Liang Y. (2012) A comparative study of melt-rock reactions in the mantle: laboratory dissolution experiments and geological field observations. *Contrib. Miner. Petrol.* **163**, 861–876.

Vauchez A., Dineur F. and Rudnick R. (2005) Microstructure, texture and seismic anisotropy of the lithospheric mantle above a mantle plume: insights from the Labait volcano xenoliths (Tanzania). *Earth Planet. Sci. Lett.* **232**, 295–314.

Vauchez A., Tommasi A., Barruol G. and Maumus J. (2000) Upper mantle deformation and seismic anisotropy in continental rifts. *Phys. Chem. Earth Part A* **25**, 111–117.

von Seckendorff V. and O'Neill H. S. C. (1993) An experimental study of Fe-Mg partitioning between olivine and orthopyroxene at 1173, 1273 and 1423 K and 1.6 GPa. *Contrib. Miner. Petrol.* **113**, 196–207.

Wagner L. S., Anderson M. L., Jackson J. M., Beck S. L. and Zandt G. (2008) Seismic evidence for orthopyroxene enrichment in the continental lithosphere. *Geology* **36**, 935–938.

Warren J. M. (2016) Global variations in abyssal peridotite compositions. *Lithos* **248**, 193–219.

Warren J. M. and Hauri E. H. (2014) Pyroxenes as tracers of mantle water variations. *J. Geophys. Res. Solid Earth* **119**, 1851–1881.

Wen D.-P., Wang Y.-F., Zhang J.-F. and Jin Z.-M. (2018) Anisotropic growth of olivine during crystallization in basalts from Hawaii: implications for olivine fabric development. *Am. Mineral.* **103**, 735–741.

Wessel P., Sandwell D. T. and Kim S.-S. (2010) The global seamount census. *Oceanography* **23**, 24–33.

Wheeler J., Prior D., Jiang Z., Spiess R. and Trimby P. (2001) The petrological significance of misorientations between grains. *Contrib. Miner. Petrol.* **141**, 109–124.

Wilde S. A., Zhou X., Nemchin A. A. and Sun M. (2003) Mesozoic crust-mantle interaction beneath the North China craton: a consequence of the dispersal of Gondwanaland and accretion of Asia. *Geology* **31**, 817–820.

Willbold M. and Stracke A. (2010) Formation of enriched mantle components by recycling of upper and lower continental crust. *Chem. Geol.* **276**, 188–197.

Wilshire H. and Shervais J. (1975) *Al–augite and Cr–diopside ultramafic xenoliths in basaltic rocks from western United States. Physics and Chemistry of the Earth*. Elsevier, pp. 257–272.

Wölbern I., Rümpker G., Link K. and Sodoudi F. (2012) Melt infiltration of the lower lithosphere beneath the Tanzania craton and the Albertine rift inferred from S receiver functions. *Geochem. Geophys., Geosyst.* **13**.

Xu Y. (2002) Evidence for crustal components in the mantle and constraints on crustal recycling mechanisms: pyroxenite xenoliths from Hannuoba, North China. *Chem. Geol.* **182**, 301–322.

Xu Y.-G., Blusztajn J., Ma J.-L., Suzuki K., Liu J.-F. and Hart S. R. (2008) Late Archean to Early Proterozoic lithospheric mantle beneath the western North China craton: Sr–Nd–Os isotopes of peridotite xenoliths from Yangyuan and Fansi. *Lithos* **102**, 25–42.

Yang J.-H., Wu F.-Y. and Wilde S. A. (2003) A review of the geodynamic setting of large-scale Late Mesozoic gold mineralization in the North China Craton: an association with lithospheric thinning. *Ore Geol. Rev.* **23**, 125–152.

Yang X., Liu D. and Xia Q. (2014) CO2-induced small water solubility in olivine and implications for properties of the shallow mantle. *Earth Planet. Sci. Lett.* **403**, 37–47.

Yang X.-Z., Xia Q.-K., Deloule E., Dallai L., Fan Q.-C. and Feng M. (2008) Water in minerals of the continental lithospheric mantle and overlying lower crust: a comparative study of peridotite and granulite xenoliths from the North China Craton. *Chem. Geol.* **256**, 33–45.

Zaffarana C., Tommasi A., Vauchez A. and Grégoire M. (2014) Microstructures and seismic properties of south Patagonian mantle xenoliths (Gobernador Gregores and Pali Aike). *Tectonophysics* **621**, 175–197.

Zhou M. F., Robinson P. T. and Bai W. J. (1994) Formation of podiform chromitites by melt/rock interaction in the upper mantle. *Miner. Deposita* **29**, 98–101.

Zhu B. (1998) *Theory and Applications of Isotope Systematics in Geosciences: Evolution of Continental Crust and Mantle in China*. Chinese, Sci Press, Beijing.

Associate editor: Fang-Zhen Teng